WEIGHING "EL GORDO" WITH A PRECISION SCALE: *HUBBLE SPACE TELESCOPE* WEAK-LENSING ANALYSIS OF THE MERGING GALAXY CLUSTER ACT-CL J0102−4915 AT $z = 0.87$

M. JAMES JEE[1], JOHN P. HUGHES[2], FELIPE MENANTEAU[2,3,4], CRISTÓBAL SIFÓN[5], RACHEL MANDELBAUM[6],
L. FELIPE BARRIENTOS[7], LEOPOLDO INFANTE[7], AND KAREN Y. NG[1]

[1] Department of Physics, University of California, Davis, One Shields Avenue, Davis, CA 95616, USA
[2] Department of Physics & Astronomy, Rutgers University, 136 Frelinghysen Rd., Piscataway, NJ 08854, USA
[3] National Center for Supercomputing Applications, University of Illinois at Urbana-Champaign, 1205 W. Clark St., Urbana, IL 61801, USA
[4] Department of Astronomy, University of Illinois at Urbana-Champaign, 1002 W. Green St, Urbana, IL 61801, USA
[5] Leiden Observatory, Leiden University, P.O. Box 9513, NL-2300 RA Leiden, Netherlands
[6] Department of Physics, Carnegie Mellon University, Pittsburgh, PA 15213, USA
[7] Departamento de Astronomía y Astrofísica, Facultad de Física, Pontícia Universidad Católica de Chile, Casilla 306, Santiago 22, Chile

ABSTRACT

We present a *Hubble Space Telescope* weak-lensing study of the merging galaxy cluster "El Gordo" (ACT-CL J0102−4915) at $z = 0.87$ discovered by the Atacama Cosmology Telescope (ACT) collaboration as the strongest Sunyaev–Zel'dovich decrement in its ∼1000 deg^2 survey. Our weak-lensing analysis confirms that ACT-CL J0102−4915 is indeed an extreme system consisting of two massive ($\gtrsim 10^{15}\ M_\odot$ each) subclusters with a projected separation of ∼0.7 h_{70}^{-1} Mpc. This binary mass structure revealed by our lensing study is consistent with the cluster galaxy distribution and the dynamical study carried out with 89 spectroscopic members. We estimate the mass of ACT-CL J0102−4915 by simultaneously fitting two axisymmetric Navarro–Frenk–White (NFW) profiles allowing their centers to vary. We use only a single parameter for the NFW mass profile by enforcing the mass–concentration relation from numerical simulations. Our Markov-Chain-Monte-Carlo analysis shows that the masses of the northwestern (NW) and the southeastern (SE) components are $M_{200c} = (1.38 \pm 0.22) \times 10^{15}\ h_{70}^{-1}\ M_\odot$ and $(0.78 \pm 0.20) \times 10^{15}\ h_{70}^{-1}\ M_\odot$, respectively, where the quoted errors include only 1σ statistical uncertainties determined by the finite number of source galaxies. These mass estimates are subject to additional uncertainties (20%–30%) due to the possible presence of triaxiality, correlated/uncorrelated large scale structure, and departure of the cluster profile from the NFW model. The lensing-based velocity dispersions are 1133^{+58}_{-61} km s^{-1} and 1064^{+62}_{-66} km s^{-1} for the NW and SE components, respectively, which are consistent with their spectroscopic measurements (1290 ± 134 km s^{-1} and 1089 ± 200 km s^{-1}, respectively). The centroids of both components are tightly constrained (∼4″) and close to the optical luminosity centers. The X-ray and mass peaks are spatially offset by ∼8″ (∼62 h_{70}^{-1} kpc), which is significant at the ∼2σ confidence level. The mass peak, however, does not lead the gas peak in the direction expected *if* we are viewing the cluster soon after first core passage during a high speed merger. Under the assumption that the merger is happening in the plane of the sky, extrapolation of the two NFW halos to a radius $r_{200a} = 2.4\ h_{70}^{-1}$ Mpc yields a combined mass of $M_{200a} = (3.13 \pm 0.56) \times 10^{15}\ h_{70}^{-1}\ M_\odot$. This extrapolated total mass is consistent with our two-component-based dynamical analysis and previous X-ray measurements, projecting ACT-CL J0102−4915 to be the most massive cluster at $z > 0.6$ known to date.

1. INTRODUCTION

One of the fundamental questions in modern cosmology is how do the large scale structures of the universe form and evolve. Galaxy clusters are the largest structures of the universe detached from the Hubble flow and gravitationally bound. Advancement in observational techniques over the past few decades has enabled us to map the distributions of the three different cluster constituents, namely, galaxies, hot plasma, and dark matter in such detail that the comparison of their distributions reveals on-going activities. These studies strongly suggest that almost all galaxy clusters possess hints of current merging activities, which is consistent with our theoretical understanding that galaxy clusters constantly grow by accreting new galaxies/groups/clusters along their neighboring filaments.

Within the hierarchical structure formation paradigm, merging is the primary mechanism for structures to grow, and thus detailed studies of cluster mergers provide key information to advance our understanding of the large-scale structure evolution of the universe. Apart from the cosmological context, merging clusters also serve as useful astrophysical laboratories, where physical properties of galaxies, intracluster gas, and dark matter can be probed. Although still in their infancy, numerical studies of merging clusters or cluster substructures will soon play pivotal roles in our understanding of properties of dark matter (e.g., Randall et al. 2008; Rocha et al. 2013).

Cluster collisions are not rare. However, enlarging the sample of prominent colliding clusters at close separation is not easy because of the limited observational time window (a few Gyr) in which to catch the merger. In addition, high-resolution X-ray imaging is required to reliably confirm the stage of the merger either through the temperature structure or offsets between galaxies and plasma. To date, only a handful of clusters are known to possess merging features convincingly indicative of
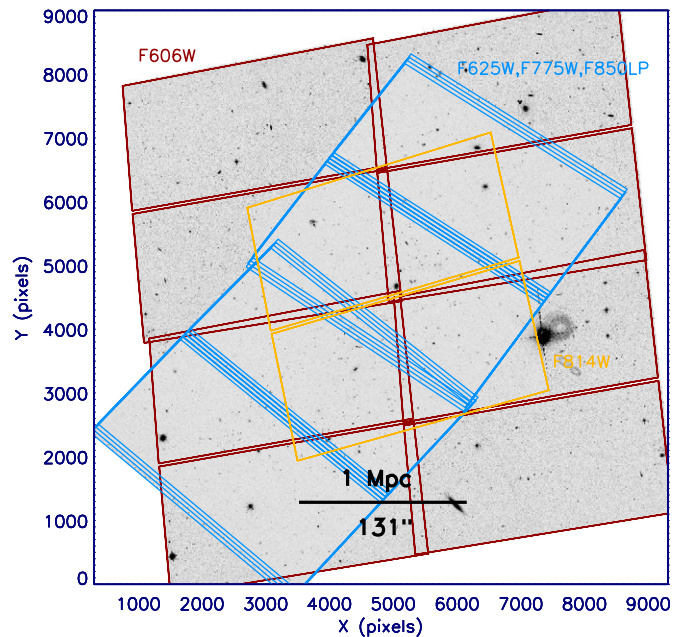
a recent core pass-through (e.g., Markevitch et al. 2002, 2005; Dawson et al. 2012; Merten et al. 2011).

The galaxy cluster ACT-CL J0102−4915 at $z = 0.87$, recently discovered as the most significant Sunyaev–Zel'dovich (SZ) decrement by the Atacama Cosmology Telescope (ACT) collaboration (Marriage et al. 2011), is a new example of this rare class of cluster. The cluster is particularly interesting because several lines of evidence indicate that the system might be a high-redshift analog of the "Bullet Cluster" (1E0657-56) at $z = 0.3$ (Markevitch et al. 2002; Clowe et al. 2006). Menanteau et al. (2012, hereafter M12) suggest that the cool peak of the X-ray emission, whose Fe abundance is substantially enhanced with respect to the rest of the cluster, may correspond to the "bullet" of the Bullet Cluster. Also, M12 find that the plasma temperature structure is reminiscent of shock heating. Moreover, their radio data analysis shows the presence of an intense double radio relic, which has now been confirmed by higher resolution, multi-frequency radio imaging (Lindner et al. 2013).

Now the conspicuously missing information, which prevents us from a deeper understanding of the system, is the underlying dark matter distribution. Therefore, in this paper we present a high-resolution weak-lensing analysis of the cluster with *Hubble Space Telescope* (*HST*) imaging. If the cluster is indeed a post-collision system of two massive clusters as suggested by M12, we expect to observe two corresponding mass clumps as in the Bullet Cluster. Also, it will be interesting to examine if we can detect a similar offset between dark matter and plasma, which has been used as direct evidence for the presence of collisionless dark matter in the Bullet Cluster. Of course, the mass will be one of the key "ingredients" necessary to set up the initial conditions for follow-up numerical studies.

Another critical discussion that this weak-lensing study can facilitate is our understanding of the cosmological implication of ACT-CL J0102−4915. Discovery of even a single sufficiently massive cluster at high redshift can provide a non-negligible challenge to the currently accepted and well tested ΛCDM structure formation paradigm if the probability of finding such a cluster within the survey is extremely small (e.g., Brodwin et al. 2012; Stanford et al. 2012; Jee et al. 2009; Foley et al. 2011; Planck Collaboration et al. 2011). As noted above, ACT-CL J0102−4915 is the most significant SZ decrement in the ACT survey, which covers nearly 1000 deg^2 (Hasselfield et al. 2013). In addition, both the South Pole Telescope (SPT) and the *Planck* data confirm that the cluster is an extreme case (Williamson et al. 2011; Planck Collaboration et al. 2013a). It has been argued, based on the strength of the SZ signal, the dynamical velocity dispersion ($\sigma_v = 1321 \pm 106$ km s^{-1}), integrated X-ray temperature $T_X = 14.5 \pm 1.0$ keV, and X-ray luminosity $L_X \sim 2 \times 10^{45}$ erg s^{-1} (in the 0.5–2.0 keV band), that ACT-CL J0102−4915 might be the most massive cluster known to date at $z > 0.6$ (M12). However, for such an extreme merger system conversion of these mass proxy measurements to actual mass estimates may not be completely reliable. Thus, our weak gravitational lensing analysis of ACT-CL J0102−4915, which does not depend on the detailed physics of the cluster baryons, provides an independent comparison to these previous non-lensing-based mass estimates. Recently Zitrin et al. (2013) presented a strong gravitational lensing analysis of ACT-CL J0102−4915 which revealed its binary mass distribution and presented a total mass estimate of $M_{200} \sim 2.3 \times 10^{15} M_\odot$.

The format of this paper is as follows. In Section 2, we describe our *HST* data. Both theoretical background and technical

Figure 1. Layout of the ACS pointings for the observation of ACT-CL J0102−4915. The F606W imaging (PROP 12477) covers the ∼6′ × 6′ area in a 2 × 2 mosaic pattern. The F625W, F775W, and F850LP filters (PROP 12755) image the ∼6′ × 3′ strip containing the two cluster galaxy overdensity regions. Only a single pointing is used for F814W (PROP 12477).

(A color version of this figure is available in the online journal.)

issues on weak-lensing are presented in Section 3. We show our mass reconstruction and provide weak-lensing mass estimates in Section 4. Section 5 presents our interpretation of the weak-lensing results in the context of the cluster merger and the cosmology. We conclude in Section 6. Unless otherwise indicated, we assume a cosmology, where $\Omega_M = 0.3$, $\Omega_\Lambda = 0.7$, and $H_0 = 70\, h_{70}$ km s^{-1} Mpc^{-1}. We use the AB magnitude system throughout and quote all uncertainties at the 1σ confidence level.

2. OBSERVATIONS

The galaxy cluster ACT-CL J0102−4915 has been observed with the *HST* under programs PROP 12755 (PI: J. Hughes) and PROP 12477 (PI: W. High). The weak-lensing analysis presented in this paper is based on our combined analysis of the data obtained under these two programs.

ACT-CL J0102−4915 was observed on 2012 September and October with the Wide Field Channel (WFC) of ACS. In PROP 12755, two ACS pointings in F625W, F775W, and F850LP were used to image a ∼6′ × 3′ strip in the NW–SE orientation to cover the two dominant substructures of ACT-CL J0102−4915 traced by the cluster galaxy distribution (M12). PROP 12477 observed the cluster in the 2 × 2 mosaic pattern with F606W and in a single pointing with F814W. The total integration per pointing is 1920 s, 2344 s, 2512 s, 1916 s, and 2516 s for F606W, F625W, F775W, F814W, and F850LP, respectively. Figure 1 illustrates the different pointings of the two *HST* programs.

We measure galaxy shapes in F606W, F625W, F775W, and F814W and combine the results wherever multiple shapes are available. Although measuring shapes in F850LP is possible, it is not optimal. This filter's point-spread function (PSF) is larger and it has a peculiar horizontal spike due to the

anti-halation layer (Jee et al. 2007a), resulting in significantly larger ellipticity errors.

Our data reduction starts with the FLC images provided by the STScI pipeline, which removes bias striping noise from post-Servicing Mission 4 images and corrects for charge transfer inefficiency (CTI) using the latest pixel-based method (Anderson & Bedin 2010; Ubeda & Anderson 2012); CTI occurs because of charge traps in the CCD, and we provide somewhat detailed discussions in Section 3.2 and Appendix A of the influence of CTI on our study. In summary, our tests show that the current level of the STScI pixel-based correction for the CTI problem is sufficient for our weak-lensing analysis.

We compute and refine World Coordinate System (WCS) offsets between different pointings by cross-correlating common astronomical sources. We estimate that the mean image registration error is ∼0.01 pixels (i.e., the average alignment error divided by the square root of the number of common objects), which would induce an ellipticity bias of ∼10^{-3} for the smallest galaxies that we use for lensing analysis. This accuracy surpasses the current weak-lensing requirement. We perform cosmic ray removal, sky subtraction, and image combination using the MultiDrizzle (Koekemoer et al. 2002) software with the "Lanczos3" drizzling kernel and an output pixel scale of 0″.05. This combination of drizzling kernel and pixel scale has been shown to provide de-facto the sharpest PSF with minimal noise correlations in our previous weak-lensing studies (e.g., Jee et al. 2007a, 2009, 2011).

Note that some weak-lensing studies (e.g., COSMOS; Koekemoer et al. 2007) prefer the "Gauss" drizzling kernel with an output pixel scale of 0″.03 arguing that the choice reduces the effects of aliasing although the resulting image shows more correlated noise between pixels. Our experiment shows that both schemes (i.e., 0″.03 with the Gauss kernel versus 0″.05 with the Lanczos3 kernel) produce very similar results in the weak-lensing analysis of ACT-CL J0102−4915. Readers are referred to Appendix B for the description of our comparison.

We create a detection image by weight-averaging all five filter images. Objects are detected with SExtractor (Bertin & Arnouts 1996) run in a dual-image mode. We identify sources by looking for at least 10 connected pixels above 1.5 times the sky rms. The total number of detected sources is ∼12,228 within the ∼6′ × 6′ area. Along the boundaries of the ACS observation footprints, some sources are clipped and contaminated by cosmic rays. We use SExtractor's FLAGS to discard the clipped objects. For cosmic rays along the boundaries, we visually scan the images and manually identify corrupted objects. After applying our source selection criteria (Section 3.5), the number density of sources is ∼101 arcmin^{-2}. Smaller weights are applied to fainter sources in our weak-lensing analysis, and thus the effective number density is slightly smaller (∼11%) than this value.

3. ANALYSIS

3.1. Theoretical Background

The transformation of a galaxy image by weak gravitational lensing is described by the following equation:

$$\mathbf{A} = (1 - \kappa) \begin{pmatrix} 1 - g_1 & -g_2 \\ -g_2 & 1 + g_1 \end{pmatrix}, \tag{1}$$

where κ is the projected mass density in units of the critical surface density Σ_c and g is the reduced shear $g = \gamma/(1 - \kappa)$.

The critical surface density is given by

$$\Sigma_c = \frac{c^2}{4\pi G D_l \beta}, \tag{2}$$

where c is the speed of light, G is the gravitational constant, and D_l is the angular diameter distance to the lens. In Equation (2), β is the distance ratio D_{ls}/D_s, where D_{ls} and D_s are the angular diameter distances between the lens and the source, and between the observer and the source, respectively. Because source galaxies are at different redshifts, it is necessary to define an effective redshift of the source plane to estimate β (Section 3.5).

According to Equation (1), a circular image is transformed into an ellipse, whose ellipticity is defined as

$$g = \left(g_1^2 + g_2^2\right)^{1/2} = (1 - r)/(1 + r), \tag{3}$$

where r is the aspect ratio of the semi-minor axis to the semi-major axis. The position angle of the ellipse is $(1/2)\tan^{-1}(g_2/g_1)$. In practice, measurement of the weak-lensing signal is much more complicated because (1) galaxy shapes possess intrinsic ellipticity, (2) imperfect charge transfers elongate object ellipticity in the readout direction, (3) the PSFs bias/dilute the signal, (4) sources are at different redshifts, (5) galaxy morphology affects the response to shear (often referred to as shear responsivity), etc. In this paper, all these subtleties are addressed in detail.

3.2. CTI Correction

In a CCD, electrons are transferred pixel-to-pixel to the readout register. However, because of defects in the silicon, some fraction of electrons remain trapped and are released after a characteristic time delay τ. This unfortunate fractional charge transfer lapse happens in every pixel-to-pixel transfer, and can be visually identified as long trails along the readout direction. Although almost every CCD is subject to this CTI, in particular this is a non-trivial issue for the *HST* detectors exposed to constant space radiation leading to considerable charge trap creation over time. In addition, the WFC detector of ACS consists of two large-format CCDs (4096 × 2048), which causes significant CTI effects for the pixels farthest from the readout register compared to the Wide Field Planetary Camera 2 comprised of relatively small (800 × 800) CCDs.

Our *HST*/ACS data of ACT-CL J0102−4915 were taken more than 10 yr after the instrument was installed in 2002 March. Therefore, the cumulative damage on the CCDs is severe, and the resulting CTI is one of our initial concerns for the use of the ACS instrument in weak-lensing studies. However, we find that the most recent pixel-based method by Ubeda & Anderson (2012) corrects for the CTI robustly to the extent that the residual shear systematic error is less than $\delta\gamma < 0.01$. Compared to the level of the statistical noise and the large lensing signal, we conclude that this level of systematic error is negligible. Our detailed discussion on this issue is presented in Appendix A.

3.3. PSF Modeling

One of the most critical instrumental signatures for weak-lensing analysis is the PSF. An anisotropic PSF distorts the images of galaxies and induces coherent ellipticity alignments, mimicking gravitational lensing. In addition, PSF blurring dilutes the apparent ellipticity. The removal of these two PSF

effects in the shear measurement is discussed in Section 3.4. Here, we focus on modeling of the PSF for ACS.

In general, the number of high signal-to-noise (S/N) stars within an ACS field is too small to describe the complicated spatial variation of the ACS PSF (Jee et al. 2007a). Because of the so-called "focus breathing," the *HST* PSF is also time-dependent. Potentially, these obstacles prevent us from modeling the PSF accurately in the region, where no nearby stars are usable to infer the PSF. However, fortunately, the *HST* PSF pattern is repetitive (Jee et al. 2007a), and this allows us to construct a PSF library from dense stellar field observations and apply the library to the weak-lensing field.

Finding a good PSF template that closely matches one's target frame is important. With simulations using *HST*/ACS globular cluster data, Jee et al. (2007a) demonstrated that the success rate is over 90% when the second moments of ~10 (out of ~1000) bright stars (S/N > 20) are used, where the matching is considered a success if the resulting residual (data-model) PSF ellipticity correlation computed from all (~1000) bright stars is less than 10^{-5}. This is a conservative criterion given the small size of the *HST* PSF.

The current mosaic image of ACT-CL J0102−4915 consists of multiple pointings, and each pointing is comprised of short (~500 s) exposures. Because our weak-lensing shapes are measured on the mosaic image (not on the individual exposure data), it is important to combine our PSF models for all individual exposures in such a way that the stacked PSF at the galaxy location is robustly represented. Therefore, we carefully trace the image registration procedures including the choice of drizzling kernel and pixel scale, the shift and rotation, and the weight distribution. We achieve an rms scatter of the residual PSF ellipticity of ~0.008. This small level of scatter is more than sufficient for the current cluster weak-lensing analysis. The PSF library of Jee et al. (2007a) is publicly available.[8]

3.4. Shear Measurement

We measure galaxy ellipticity by fitting an elliptical Gaussian to pixellated images. The resulting semi-major and -minor axes, a and b, and orientation ϕ are used to define the following e_1 and e_2 components:

$$e_1 = e \cos 2\phi, \tag{4}$$

$$e_2 = e \sin 2\phi, \tag{5}$$

where

$$e = \frac{a - b}{a + b}. \tag{6}$$

Because observed galaxy images are smeared by PSFs, we convolve the elliptical Gaussian by model PSFs prior to fitting. This so-called "forward modeling" removes both anisotropic and smearing effects of the PSF by performing this indirect deconvolution. Other techniques include moment-based methods such as Kaiser et al. (1995), which performs quasi-deconvolution using moments of both stars and galaxies to remove these PSF effects.

Although the anisotropic PSF effect is taken care of by the above forward modeling, our shear measurement with the above method is still subject to a multiplicative bias, which means that the raw ellipticity should be multiplied by a calibration factor (higher than unity) to match gravitational shear.

This is because (1) the exact ellipticity transformation rule for a given shear γ depends on the galaxy surface brightness profile (morphology-dependent shear responsivity), (2) galaxy surface brightness profiles are not Gaussian (model incompleteness), (3) ellipticity measurement is a non-linear mapping, (4) galaxies possess their own intrinsic ellipticities associated with their formation environment (intrinsic alignment). Issues (1), (2), and (3) can be addressed both analytically (Bernstein & Jarvis 2002) and numerically (through image simulations). In Jee et al. (2013), we find that the simple analytic recipe of Bernstein & Jarvis (2002) agrees reasonably well with our image simulation result for bright galaxies. However, the difference is large for low S/N galaxies. This S/N-dependent bias (so-called "noise bias") is an important issue for future cosmic shear surveys (Melchior & Viola 2012; Refregier et al. 2012). In this paper, we address this shear calibration through image simulations and determine the calibration factor. This type of shear calibration also takes care of the impact of systematics due to neighboring objects statistically because we ensure the number density of simulated objects to match observed values. Our calibration factor varies from ~1.05 to ~1.16 depending on the S/N value of the object. Although in principle, one can use S/N-dependent calibration, we find that for the current weak-lensing analysis it is sufficient to apply a global factor ~1.11 (our ellipticities should be multiplied by 1.11 to give shear) to the entire source population; the difference in the final result is only at the sub-percent level. However, we note that in future cosmic shear surveys it is critical to use S/N-dependent calibration because the S/N-dependence implies also redshift-dependence. The intrinsic alignment (4) is an important topic again in cosmic shear studies. However, this can safely be ignored in the current cluster lensing, where the strength of the lensing signal is a few orders-of-magnitude higher than intrinsic alignment signals (e.g., Hao et al. 2011; Schneider et al. 2013).

We measure object ellipticities in F606W, F625W, F775W, and F814W. Where available, ellipticities from different colors are combined; we found no statistically significant difference in galaxy shapes among different filters. We use inverse-variances derived from ellipticity errors as weights. Combining shapes from different filters allows us to use fainter galaxies for our weak-lensing than using shapes from a single filter. For example, when we use shapes only from F775W, the number density of sources is ~93 arcmin^{-2} within the $6' \times 3'$ strip (after applying our source selection criteria described in Section 3.5). Adding the shapes from F606W, F625W, and F814W increased the source number density to ~101 arcmin^{-2}.

These raw numbers should not be confused with effective number densities. Effective number densities are the results that we obtain after taking into account the fact that fainter sources provide noisier measurements and thus are de-weighted. We define our weight as
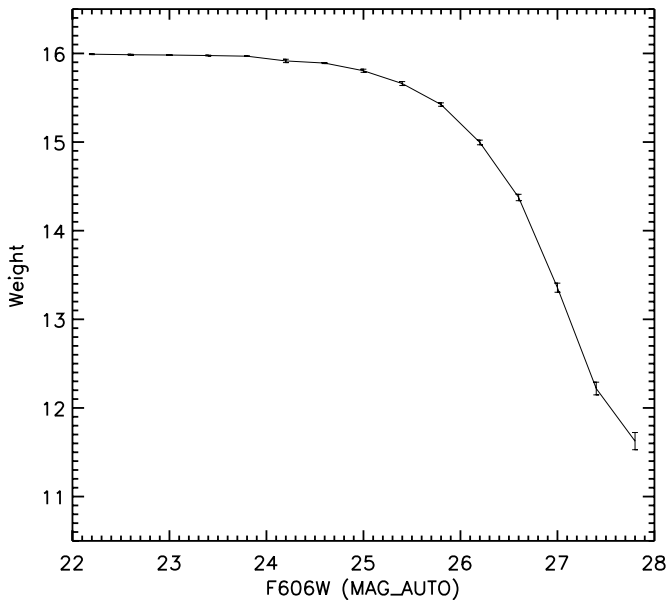
$$\mu_i = \frac{1}{\sigma_{SN}^2 + (\delta e_i)^2}, \tag{7}$$

where σ_{SN} is the shape noise (~0.25) and δe_i is the measurement error for the ith galaxy. Then, the corresponding n_{eff} is

$$n_{eff} = \frac{1}{A} \sum \frac{\sigma_{SN}^2}{\sigma_{SN}^2 + (\delta e_i)^2}, \tag{8}$$

where A is the field area. According to the above weighting scheme, n_{eff} is ~90 sources arcmin^{-2}, ~11% smaller than the

---

Figure 2. Magnitude vs. ellipticity weight. We display our ellipticity weight (Equation (7)) as a function of the F606W magnitude.

raw number density ~ 101 arcmin^{-2}. We display in Figure 2 our relation between source magnitude and weight.
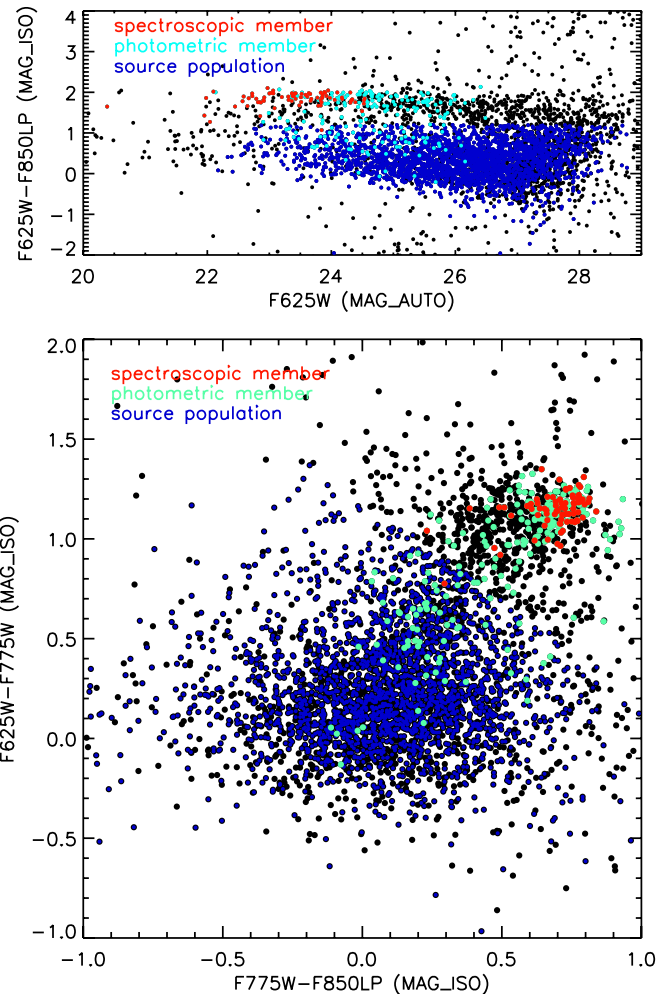
3.5. Source Selection and Redshift Estimation

We combine imaging data from two programs, and this somewhat complicates source selection and their redshift estimation. The $6' \times 3'$ stripe area (hereafter Region A) observed by PROP 12755 is imaged in F625W, F775W, and F850LP. Thus, it is possible to employ the traditional red-sequence technique to identify and remove cluster galaxies in this region based on the ACS data. However, about 48% of our target area is observed only with F606W (hereafter Region B). For this region, we can remove only bright cluster galaxies utilizing the photometric redshift catalog of M12. Fortunately, since Region B is far from the cluster center, the expected number of cluster galaxies is small. Furthermore, because the lensing signal is much weaker than in Region A, less stringent contamination rate (and source redshift) estimation is required for our weak-lensing analysis of the cluster.

3.5.1. Region A

We rely on the traditional method, which discards cluster members identified through their 4000 Å break feature. Although it is a powerful method to select "red" cluster galaxies, the procedure includes a significant fraction of non-background galaxies into the source catalog. We quantify the dilution of the lensing signal due to this contamination statistically, utilizing a high-fidelity photometric redshift catalog obtained from control fields.

The redshifted 4000 Å break at $z = 0.87$ (~ 7480 Å) is well-bracketed by F625W and F850LP. In the top panel of Figure 3, the color–magnitude diagram clearly shows the red-sequence cluster galaxies of ACT-CL J0102−4915 (the F625W−F850LP color of the bright end is ~ 2). We define our source galaxies as the population bluer than this red-sequence in the magnitude range $22 < \text{F775W} < 28$. In addition, we use the photometric redshift catalog of M12 to identify and remove blue cluster members.
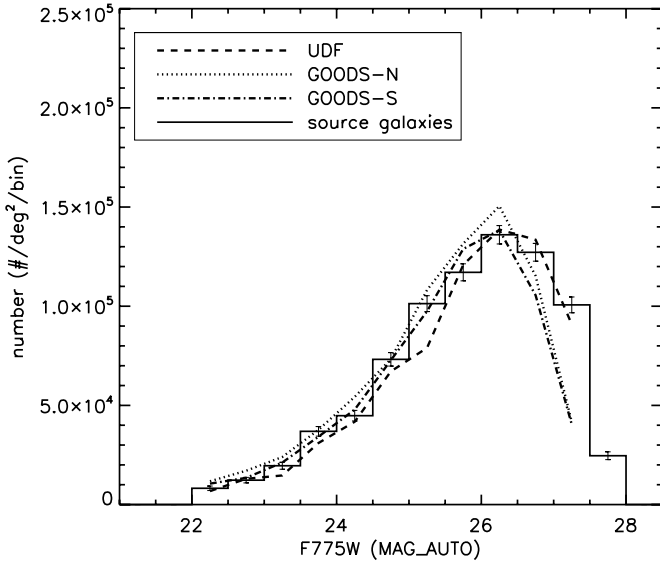

Figure 3. Source galaxy selection. Top: color–magnitude relation. The locus of the red-sequence is clearly visible down to F625W ~ 26. This color–magnitude relation is used to select our sources (blue). Bottom: color–color relation. We considered using a color–color diagram for source selection. However, compared to the color–magnitude diagram (top), this scheme does not provide an advantage over the red-sequence method for the current data set. The red-sequence is already well-separated with the color magnitude diagram. The blue cluster member candidates are severely blended with our source population.

(A color version of this figure is available in the online journal.)

The blue points in Figure 3 represent the source population selected in this way. We find that only one spectroscopic member (out of 89) is included in this selection. We note, however, that we preferentially selected red galaxies for our spectroscopic follow-up. The resulting S/N threshold of the source at the faint end is about 5.

One may suggest source selection using all of the three filters (bottom panel of Figure 3). However, we find that this method does not provide advantage over the above color–magnitude relation. The red-sequence is already well-separated with the color magnitude diagram. The blue cluster candidates are severely blended with our source population in both panels.

Our source magnitude range is broad ($22 < \text{F775W} < 28$), and the choice of the upper and lower limits can be a subject for debate. Obviously, we desire to avoid the cases where the sources near the bright end are mostly foreground galaxies or where the sources near the faint end are too noisy to be used for weak-lensing studies. Our test shows that the sources at both ends possess significant lensing signals (Appendix C).

Figure 4. Magnitude distribution of source galaxies. We use the publicly available *HST* images of the UDF and GOODS data to examine a potential excess in the magnitude distribution of our source galaxies with respect to these control field galaxies. We add noise to the UDF and GOODS images to match their depth to our ACS image of ACT-CL J0102−4915. We find that the magnitude distribution of our source galaxies is similar to those from GOODS and UDF without any hint of an excess.

We applied a S/N cut by imposing that sources should have ellipticity measurement errors less than 0.25. To avoid the pixellation artifact mentioned in Jee et al. (2013), we require the semi-minor axis b (pre-seeing) to be greater than 0.4 pixels. Along with this constraint, we ensure that the half-light radius (r_h) should be greater than 1.2 pixels (larger than the PSF).

For lenses at high redshift, care must be taken in estimating source redshifts because (1) many cluster members are blue and thus their 4000 Å feature is weak, (2) the lensing signal is sensitive to source redshifts, and (3) the width of the source redshift distribution is non-negligible.

We address (1) by comparing the magnitude distribution of the source population with those from other control fields. If a significant fraction of blue cluster members is included in our source catalog from the selection procedure just described, we expect to observe an excess with respect to some control fields. We use the publicly available *HST* images of the Ultra Deep Field (UDF; Beckwith et al. 2006) and the Great Observatories Origins Deep Survey (GOODS; Giavalisco et al. 2004). Because these images are significantly deeper than the current ACT-CL J0102−4915 images, it is necessary to add noise to the control field images in order to match the depth. In addition, we need to apply the same selection criteria such as magnitude range, size, color, etc. We display the comparison in Figure 4. We find that the magnitude distribution of our source galaxies is similar to those from GOODS and UDF without any evidence for an excess from blue cluster member contamination.

Although no statistically significant excess is detected in the above comparison, the top panel of Figure 3 shows that our source selection includes some blue cluster member candidates defined by the M12 photo-z catalog. For sources with F775W < 26.5, the fraction is about ∼5%. Although negligibly small, this contamination rate is included in our source redshift estimation.

After confirming that the contamination fraction of blue cluster members in our source catalog is negligibly small, we address (2) and (3) using the UDF and GOODS photometric

redshift catalogs of Coe et al. (2006) and Dahlen et al. (2010), respectively.

The UDF photometric redshifts are derived from the ultra-deep ACS and NICMOS images. For example, the limiting AB magnitude (S/N = 10 in 0.2 arcsec^2) is ∼29 in F435W, F606W, F775W, and F850LP. This catalog has been widely applied to our previous weak-lensing studies of high-redshift clusters (e.g., Jee et al. 2011). Because the UDF field consists of a single ACS pointing ($3' \times 3'$), it does not allow us to address cosmic variance, which becomes a limiting factor in high-redshift cluster mass determination. In Jee et al. (2009), it was realized that sample variance was an important issue for deriving the mass of the then highest-redshift cluster XMMU J2235.3−2557 at $z = 1.4$. Jee et al. (2009) estimated that the uncertainty on the effective redshift of background galaxies used for their weak-lensing study was ≃0.06, based on examining two additional redshift catalogs (Hubble Deep Field North: HDF-N, and Ultra Deep Field Parallel Field: UDF-P).

Here, we expand the study of Jee et al. (2009) utilizing the photometric redshift catalog from the GOODS data. GOODS consists of two separate fields, each of which covers an area of 10×16 arcmin^2. We combine the public release of the GOODS photometric catalog version 2.0[9] with the Dahlen et al. (2010) photo-z catalog; this procedure is necessary because the photo-z catalog does not contain photometry. The combined catalog contains 37,238 and 32,508 objects for the northern and southern fields, respectively. The number density exceeds ∼200 arcmin^{-2}. This is much higher than our source density (∼100 arcmin^{-2}), although we believe that a substantial fraction of the faint GOODS galaxies may not have secure photometric redshifts. These faint sources are likely to default to a prior, for which Dahlen et al. (2010) use a luminosity function. Note that Coe et al. (2006) used the HDF-N prior for their UDF photo-z estimation.

As shown in Equation (2), the lensing signal (surface mass density) is scaled by the angular diameter ratio D_{ls}/D_s. Because sources at lower than the cluster redshift are not lensed, we compute β as follows:

$$\beta = \left\langle \max\left(0, \frac{D_{ls}}{D_s}\right) \right\rangle. \qquad (9)$$

Thus, the corresponding redshift is referred to as *effective* (rather than *mean*) source redshift. As mentioned above, we apply our source selection criteria to the UDF and GOODS galaxies. In addition, it is important to correct for the difference in depth and the magnitude-dependent weighting scheme used in shear estimation.

After taking into account these subtleties, we obtain $\beta = 0.257$ from the UDF photometric redshift catalog of Coe et al. (2006) corresponding to an effective source plane redshift $z_{\text{eff}} = 1.32$. Without the last two corrections, β would be higher by ∼4%. Substituting $\beta = 0.257$ into Equation (2) gives $\Sigma_c \simeq 4050 \, M_\odot \, \text{pc}^{-2}$. The resulting non-background contamination rate is ∼31%.

We obtain similar values from the GOODS photometric redshift catalog of Dahlen et al. (2010). The northern and southern fields yield $\beta = 0.268$ ($z_{\text{eff}} = 1.35$) and 0.262 ($z_{\text{eff}} = 1.33$), respectively. To estimate the Poisson scatter, we define 7 and 8 non-overlapping ACS pointings (i.e., size of the UDF) in the northern and southern fields, respectively, and measure

---

β from each pointing. The standard deviations in β are 0.008 and 0.005 for GOODS-N and -S, respectively. The β value from UDF is consistent with the mean value in GOODS-S and about 1σ lower than the mean value in GOODS-N. If we adopt the larger difference (between GOODS-N and UDF) as the representative scatter in β, the difference of $\Delta\beta = 0.01$ ($\Delta z_{\rm eff} \simeq 0.03$) gives rise to a $\sim4\%$ shift in mass. The small difference in β between the two GOODS fields that are widely separated on the sky is encouraging, although one has yet to establish the scatter arising from cosmic variance based on more surveys available in the future. Hereafter, we adopt the UDF photo-z result to scale our lensing signal.

As mentioned above, the width of the distribution also affects the scaling of the lensing signal. We obtain $\langle\beta^2\rangle = 0.119 \pm 0.005$. Thus, the observed reduced shear g' is related to the true reduced shear g via $g' = [1 + (\langle\beta^2\rangle/\langle\beta\rangle^2 - 1)\kappa]g \simeq (1 + 0.79\kappa)g$ (Seitz & Schneider 1997). This correction is important in the region where κ is high, and we address the effect when we fit a model to the observed cluster shear profile for our mass determination. Omission of this correction alone leads to overestimation of the cluster mass by as much as $\sim15\%$.

3.5.2. Region B

From the photo-z catalog of M12, we select 410 objects with $0.7 < z_{\rm phot} < 0.96$. Among these 410 objects, 75 sources are located in Region B. After removing these cluster member candidates, we apply the $22 < {\rm F606W} < 28$ magnitude cut. As is done for the sources in Region A, we further trim the source catalog by ensuring that the sources are sufficiently large ($b > 0.4$ and $r_h > 1.2$) and their ellipticity has a reasonable measurement uncertainty $\delta e < 0.25$.

We attempted to estimate a cluster galaxy contamination rate in these sources by comparing their magnitude distribution with those from the UDF and GOODS fields as is done for the sources in Region A. However, in contrast to our initial expectation, we cannot find any excess in Region B. We suspect that this may be because the contamination from "red" cluster members is insignificant in Region B or the source density in the field happens to be intrinsically low.

The total number of sources in Region B is 3255 (~102 arcmin^{-2}). This source density is similar to that in Region A. This may seem surprising because in Region A we combine the shapes from four different filters, which give more galaxies with smaller shape measurement errors. However, in Region A there are more cluster galaxies, which we discard. This offsets the increase due to the combination of different filters.

Using the UDF photo-z catalog of Coe et al. (2006), we obtain $\beta = 0.276$ corresponding to the effective redshift $z_{\rm eff} = 1.37$. This value is slightly higher than the estimate $z_{\rm eff} = 1.32$ in Region A. When we use the GOODS photometric redshift catalog of Dahlen et al. (2010), the north and south fields give $\beta = 0.268$ ($z_{\rm eff} = 1.34$) and 0.263 ($z_{\rm eff} = 1.33$), respectively. For our subsequent analysis, the UDF result is adopted. However, we note that these different β values causes only insignificant changes in our final weak-lensing analysis. For example, the cluster masses are affected at most by $\sim4\%$, which is much smaller than the contribution from other sources. In addition, we stress that the cluster lensing signal is dominated by the sources in Region A, although the sources in Region B helps us to reduce statistical uncertainties by allowing us to measure more robust tangential shears at large radii from complete circles.

4. RESULTS

4.1. Two-dimensional Mass Reconstruction

Weak-lensing distorts shapes of background galaxies only slightly, and thus the detection of the signal requires averaging over a number of galaxy shapes. The left panel of Figure 5 displays a so-called "whisker" plot, where each whisker represents both the direction and magnitude of the local average ellipticity. In principle, it is possible to convert this shear field into a mass distribution through the following relation:

$$\kappa(\mathbf{x}) = \frac{1}{\pi} \int D^*(\mathbf{x} - \mathbf{x}')\gamma(\mathbf{x}')d^2\mathbf{x}, \tag{10}$$
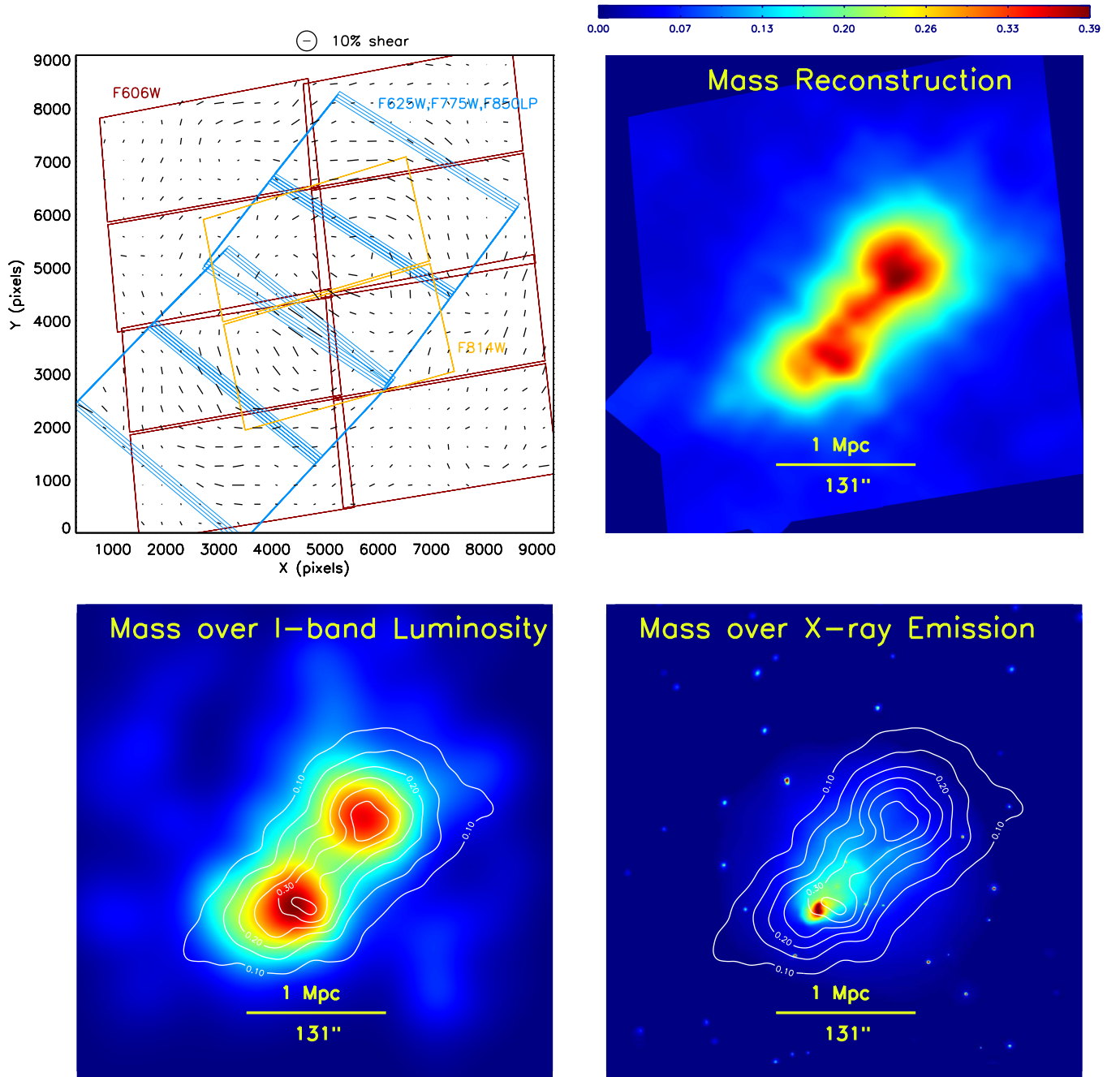
where $D(\mathbf{x}) = -1/(x_1 - ix_2)^2$ is the convolution kernel. However, the process is sensitive to noise, as is often the case with inversion problems. Many algorithms to overcome the pitfalls of this direct inversion have been suggested. In this study, we use the maximum entropy reconstruction method of Jee et al. (2007b), which revised the earlier algorithm of Seitz et al. (1998). The method implements not only the nonlinear relation between galaxy ellipticity and shear, but also the S/N-dependent smoothing of the lensing signal utilizing the entropy of the convergence values. We verify that very similar results are obtained with different mass reconstruction algorithms (e.g., Kaiser & Squires 1993; Fischer & Tyson 1997; Lombardi & Bertin 1999) except that the maximum entropy method yields the fewest spurious features near the field edges.

The uncertainties in our mass reconstruction are estimated from a Hessian matrix. The Hessian matrix is derived by taking the second derivatives of the target function (i.e., function to minimize) with respect to parameters (i.e., convergence κ). Under the assumption that the error distribution is Gaussian, we can adopt the resulting matrix elements as inverse of the covariances. Readers are referred to Bridle et al. (1998) for further details. We note that bootstrapping is not a feasible solution because our maximum entropy method is slow (several hours to converge). The resulting convergence rms map is displayed in Figure 6. The rms value ranges from $\delta\kappa \sim 0.02$ to ~0.06. Since our entropy regularization dampens possible fluctuations near the field boundaries, the rms values are much lower in those regions. This trend is reversed in mass reconstructions performed without any regularization because fewer galaxies are available near the boundaries.

Our weak-lensing analysis reveals that ACT-CL J0102$-$4915 consists of two massive subclusters separated by $\sim700\,h_{70}^{-1}$ kpc, closely resembling the cluster galaxy light distribution (see Figure 5). The shear peaks are located at R.A. = 01:02:50.60, Decl. = $-$49:15:04.5 for the NW component and R.A. = 01:02:56.31, Decl. = $-$49:16:23.2 for the SE one. This bimodal distribution can also be inferred by the whisker plot showing the tangential alignments of the sticks around these two mass clumps. The X-ray image, however, does not show any significant gas overdensity for the northwestern (NW) mass clump (the lower-right panel of Figure 5). Figure 7 summarizes the comparison of the mass centroids with the centroids of X-ray emission, number density, luminosity, and SZ decrement.

4.2. Significance and Locations of the Weak-lensing Mass Peaks

In order to investigate the statistical significance of the difference between the two mass peaks and other centroids, we measure mass peak centroids from the 1000 bootstrap runs.
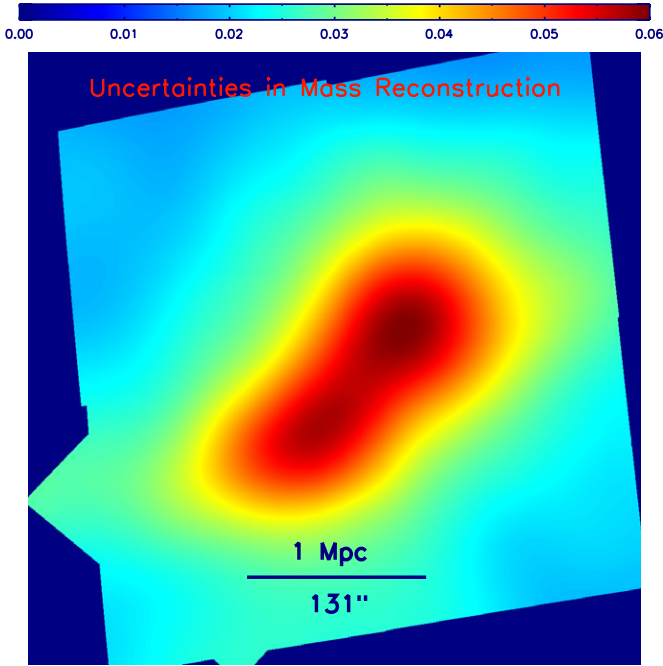
Figure 5. Two-dimensional mass reconstruction of ACT-CL J0102−4915. The "whisker" plot in the upper-left panel shows the smoothed ellipticity variation of background galaxies. The orientation and length of the sticks represent the position angle and magnitude of the ellipticity, respectively. The stick inside the circle above the plot illustrates the size of a 10% shear whereas the diameter of the circle shows the size (FWHM = 30″) of the Gaussian smoothing kernel used here. The upper-right panel displays the resulting two-dimensional mass reconstruction. We performed the mass-sheet degeneracy ($\kappa \rightarrow 1 - \lambda + \lambda\kappa$) transformation in such a way that κ becomes zero near the map boundaries. We overlay the mass contours on the smoothed optical luminosity and X-ray emission in the lower-left and -right panels, respectively.

(A color version of this figure is available in the online journal.)

We use the FIATMAP code (Fischer & Tyson 1997) to carry out this experiment. The centroid is determined by iteratively computing first moments from the convergence map. We use a FWHM = 20″ Gaussian for weighting κ. Figure 8 displays the results for both mass peaks, where the (0,0) position is referenced to the location of each component's shear peak. The peak of the NW mass clump coincides with the NW galaxy luminosity peak. Interestingly, the centroid of the SZ decrement is close to this luminosity peak, although it is unclear whether or not the SZ centroid is physically representative of the location

of the NW cluster potential well. The southeastern (SE) mass peak is close to the corresponding SE galaxy luminosity peak. The X-ray emission is strongest near this SE mass peak. The distance between the X-ray and SE mass peaks is ∼8″. Based on the above bootstrapping analysis, the significance of the offset is at the ∼2σ level. In contrast to the galaxy light distribution, the galaxy number density peaks show large offsets with respect to the mass centroids. The NW number density centroid is offset from the corresponding mass peak by ∼15″ (≳ 2σ), and the SE number density centroid is separated from the SE mass peak by

Figure 6. Convergence (κ) error distribution derived from our Hessian matrix. The rms value ranges from $\delta\kappa \sim 0.02$ to ~ 0.06. Since our entropy regularization dampens possible fluctuations near the field boundaries, the rms values are much lower in those regions. This trend is reversed in mass reconstructions performed without any regularization because fewer galaxies are available near the boundaries.
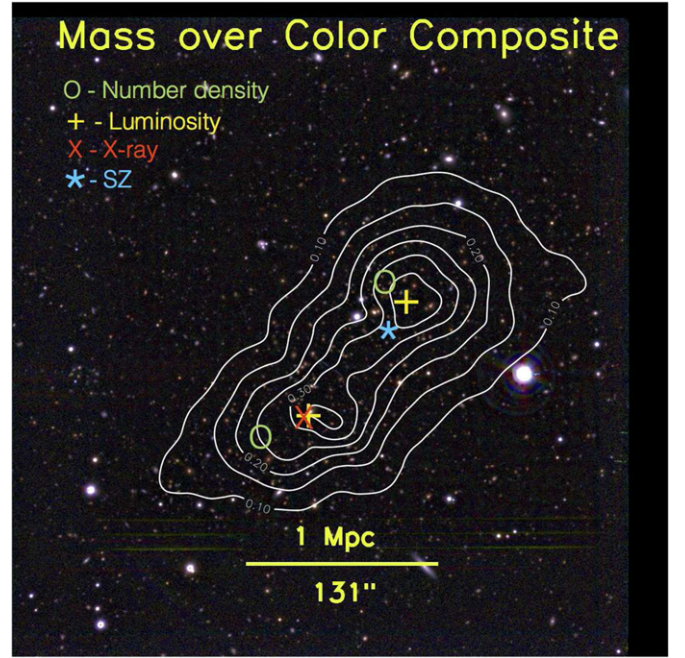
(A color version of this figure is available in the online journal.)

Figure 7. Mass contours overlaid on the VLT-SOAR color-composite image (using the z, i, and r filters for red, green, and blue, respectively). Various measures of the cluster centroids are shown as illustrated. The mass contours are depicted using solid white lines. North is up and east is left.
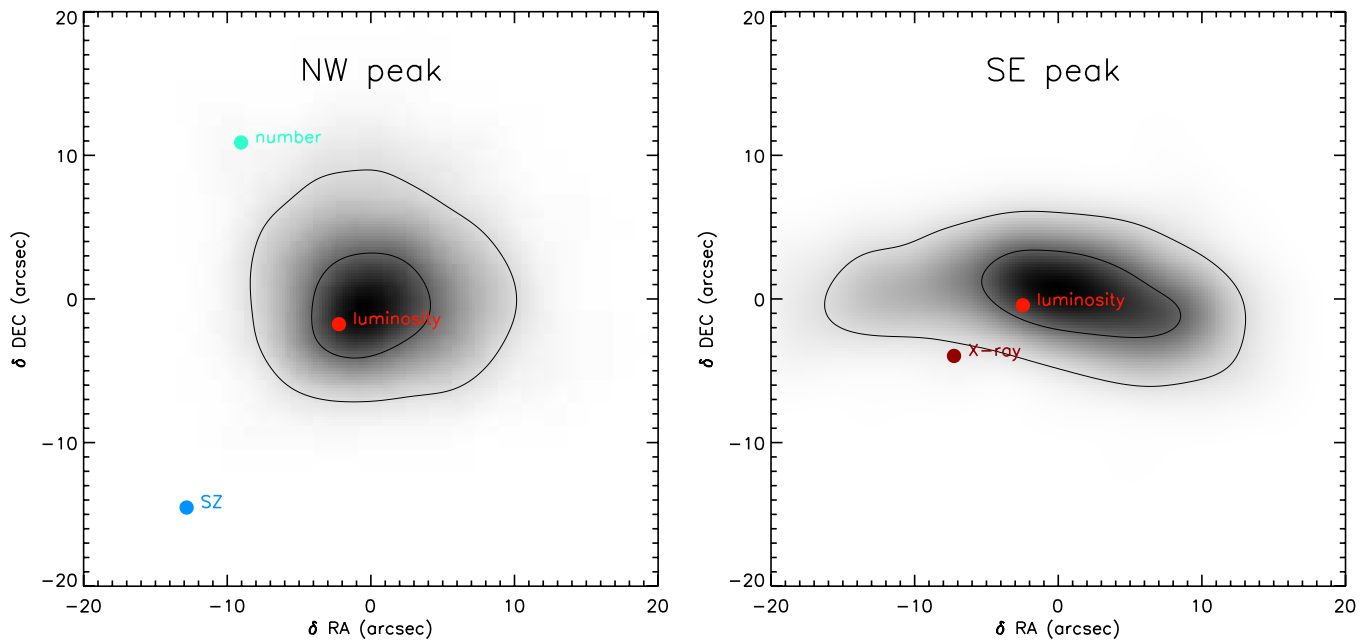
(A color version of this figure is available in the online journal.)

$\sim 400 \, h_{70}^{-1}$ kpc ($\sim 50''$), which is outside the plotting region in Figure 8.

We measure the significance of the mass peaks utilizing the rms map (Figure 6). The background level is determined within the mass reconstruction field. Because the lensing signal is still strong at the field boundary, this estimation of the significance should be regarded as conservative. As we lift the mass-sheet degeneracy by enforcing the convergence values near the field boundaries to approach zero, we effectively take into account the nonlinear $g = \gamma/(1 - \kappa)$ relation between shear and convergence. The significance of the NW mass clump ($\sim 9\sigma$ within a $r = 50''$ aperture) is slightly higher than that of the SE mass clump ($\sim 6\sigma$) and is consistent with the mass ratio of the two subclusters (see Section 4.3).

4.3. Mass Determination of ACT-CL J0102−4915

One of the most cosmologically interesting properties of ACT-CL J0102−4915 is its virial mass. The cluster redshift $z = 0.87$ approximately corresponds to half the age of the universe, and according to the standard ΛCDM prediction, the $z = 0.87$ mass function at the high end is expected to be several orders of magnitude lower than the amplitude at $z = 0$. Therefore, the cosmological leverage of ACT-CL J0102−4915 is significant *if* the mass of the cluster is indeed as high as indicated by its X-ray, SZ, and dynamical data. M12 showed that the combined mass estimate of ACT-CL J0102−4915 is near the 95% exclusion curve of Mortonson et al. (2011) when the full ACT+SPT 2800 deg^2 survey area is considered, although M12 caution that, because of the large mass uncertainty, it would be premature to regard the cluster as a challenge to the current ΛCDM paradigm.

The mass distribution of ACT-CL J0102−4915 is bimodal, and thus we must take care in determining the virial mass of the system. Because the current ACS data covers a small area, it is not feasible to use a model-independent method such as aperture mass densitometry, which requires shear measurement over a considerably larger area. Therefore, in this study we use parametric models and compare the expected shears with the observed galaxy ellipticity.

Conventionally, this parametric approach is implemented by first measuring a one-dimensional (1D) azimuthally averaged tangential shear profile around the center of each mass component and then fitting an independent model to each profile. Although our presentation below includes the results from this approach, in the study of ACT-CL J0102−4915 we regard this method as biased for the following reasons.

The main weakness of this method is that this 1D analysis assumes that there is only a single halo whereas the shapes of the source galaxies are affected by other substructures. Since ACT-CL J0102−4915 is comprised of at least two massive halos, this weak-lensing signal interference will bias the cluster mass non-negligibly, although we cannot make a general statement on the direction of the shift. Another potential issue is the sensitivity of the profile shape to the choice of the halo center. In general, choosing centers determined by mass reconstruction can bias the mass estimate high because the decision is based on the noisy realization. In this study, we assume that the luminosity peaks (Figure 7) are also the centers of the dark matter halos, which turns out to be in good agreement with the results from the two-dimensional (2D) analysis discussed below. Fortunately, in the case of ACT-CL J0102−4915, the centroid of each component is tightly constrained by the lensing.

Our second approach is to fit two model halos simultaneously to the ensemble of individual galaxy ellipticities. This overcomes the pitfalls of the first method. Now we free the

Figure 8. Bootstrapping test of centroid distribution. We use the `FIATMAP` code to carry out the experiment. The inner- and outer contours represent 1σ and 2σ limits. The centroid distribution of the SE peak is elongated east–west, which is similar to the profile of the convergence κ. The (0,0) positions correspond to positions of R.A. = 01:02:50.601, Decl. = -49:15:04.48 for the NW component and R.A. = 01:02:56.312, Decl. = -49:16:23.15 for the SE one.

(A color version of this figure is available in the online journal.)

centroid of each cluster, which explores the impacts of centroid bias in cluster mass estimation. The uncertainties of the masses obtained from this method are estimated, therefore, after marginalizing over the centroids of the two halos using a Markov-Chain-Monte-Carlo (MCMC) analysis.

Figure 9 shows the 1D tangential shear profile and the model fit results. Also displayed are the 45-deg rotation test results (diamond), which provide a useful diagnostic for residual systematics. This so-called B-mode signal does not indicate any significant residual systematics. Note that we corrected for the small difference in β when the sources in Region A and B are combined.
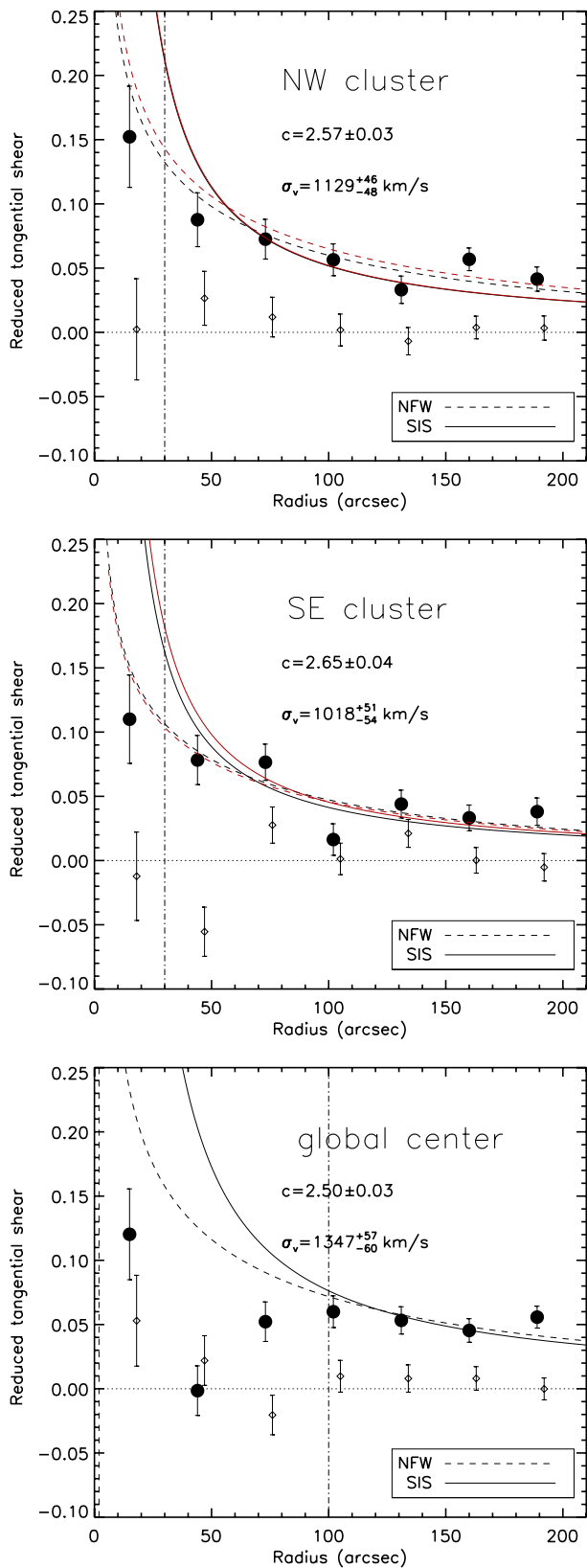
Prior to fitting, we need to exclude the shears at small radii for each halo because in this regime (1) current theory does not converge on the behavior of the halo profile, (2) the chance of cluster galaxy contamination is high, (3) the signal shape is sensitive to the choice of center, and (4) the weak-lensing assumption is not valid. Currently, no simulation-based study on the optimal choice of the cutoff radius is present. In this paper, we adopt $r = 30''$, which is greater than the expected Einstein radius ($\sim10''$) of each halo for the effective source plane redshift $z_{\rm eff} \sim 1.3$ (see Section 3.5 for our source redshift estimation).

Despite the above caveats in the 1D analysis, the amplitudes of the tangential shears in Figure 9 indicate that the two halos of ACT-CL J0102$-$4915 are indeed massive. The solid and dashed lines show our best-fit results using the singular isothermal sphere (SIS) and the Navarro–Frenk–White (NFW; Navarro et al. 1997) models. We assume the Duffy et al. (2008) mass–concentration relation in our NFW fits. The black lines are the results when we use the 1D tangential shear profiles whereas the red lines show the results from the 2D fits described below. Conversion of the SIS fit result to velocity dispersion is straightforward. From the 1D fits, the predicted velocity dispersions for the NW and SE subclusters are $\sigma_v = 1129^{+46}_{-48}$ km s^{-1} and 1018^{+51}_{-54} km s^{-1}, respectively. These values

are consistent with the dynamical (spectroscopic) measurements of 1290 ± 134 km s^{-1} and 1089 ± 200 km s^{-1} for the NW and SE components, respectively (M12). The bottom panel in Figure 9 displays the results when we measure the tangential shear around the global center of the two components. We exclude shear values at $r < 100''$ in this case. We do not claim that this cutoff radius $r = 100''$ is a legitimate choice because the interference of the lensing signal from the two subclusters should extend beyond this value; clearly, the shape of the radial profile at $r < 100''$ cannot be modeled by the profile of a single halo. For this choice of center, our 1D SIS fit predicts $\sigma_v = 1347^{+58}_{-60}$ km s^{-1}, which is also consistent with the direct measurement 1321 ± 106 km s^{-1} (M12).

From the NFW fits, we estimate $M_{200c} = (1.17 \pm 0.17) \times 10^{15} \, h_{70}^{-1} \, M_\odot$ and $(0.79 \pm 0.14) \times 10^{15} \, h_{70}^{-1} \, M_\odot$ for the NW and SE mass clumps, respectively. Note that M_{200c} refers to a mass within a sphere inside which the mean density equals 200 times the *critical* density of the universe at the cluster redshift. The circles traced by the corresponding r_{200c} values ($\sim1.6 \, h_{70}^{-1}$ Mpc and $\sim1.4 \, h_{70}^{-1}$ Mpc for the NW and SE, respectively) are greater than the size of our ACS field. Thus, a more relevant mass might be M_{500c}, whose defining radius is a factor of two smaller. Table 1 summarizes our 1D mass estimation results including these M_{500c} values.

Our full 2D analysis (simultaneous fitting of two halos with freed centroids) produces cluster mass values that are slightly different from the above 1D fitting results, although with overlapping error bars; the predicted amplitudes are compared in Figure 9. Because it is obvious that the interference of the lensing signal between the two halos is non-negligible, we are confident that this second method should produce more unbiased results. We estimate the NW and SE components' masses to be $M_{200c} = (1.38 \pm 0.22) \times 10^{15} \, h_{70}^{-1} \, M_\odot$ and $(0.78 \pm 0.20) \times 10^{15} \, h_{70}^{-1} \, M_\odot$, respectively. These values are obtained with the same ($r < 30''$) cluster-core-exclusion radius

Figure 9. Reduced tangential shear profile. Filled circles represent the tangential shear while open diamonds show the 45 deg rotation test results. The vertical dot-dashed line shows the cut-off radius, inside which the signal is not used to constrain the models. The solid and dashed lines represent the best-fit SIS and NFW models, respectively. The black lines are the results when we use this 1D tangential shear profiles whereas the red lines show the results from our simultaneous 2D fits (see text). The displayed concentration and predicted velocity dispersions are the results from the 1D fits.

(A color version of this figure is available in the online journal.)

as used in our 1D fitting. The predicted velocity dispersions are $\sigma_v = 1133^{+58}_{-61}$ km s^{-1} and 1064^{+62}_{-66} km s^{-1} for the NW and SE subclusters, which are also in good agreement with the spectroscopic measurements. We summarize our 2D fitting results in Table 2.
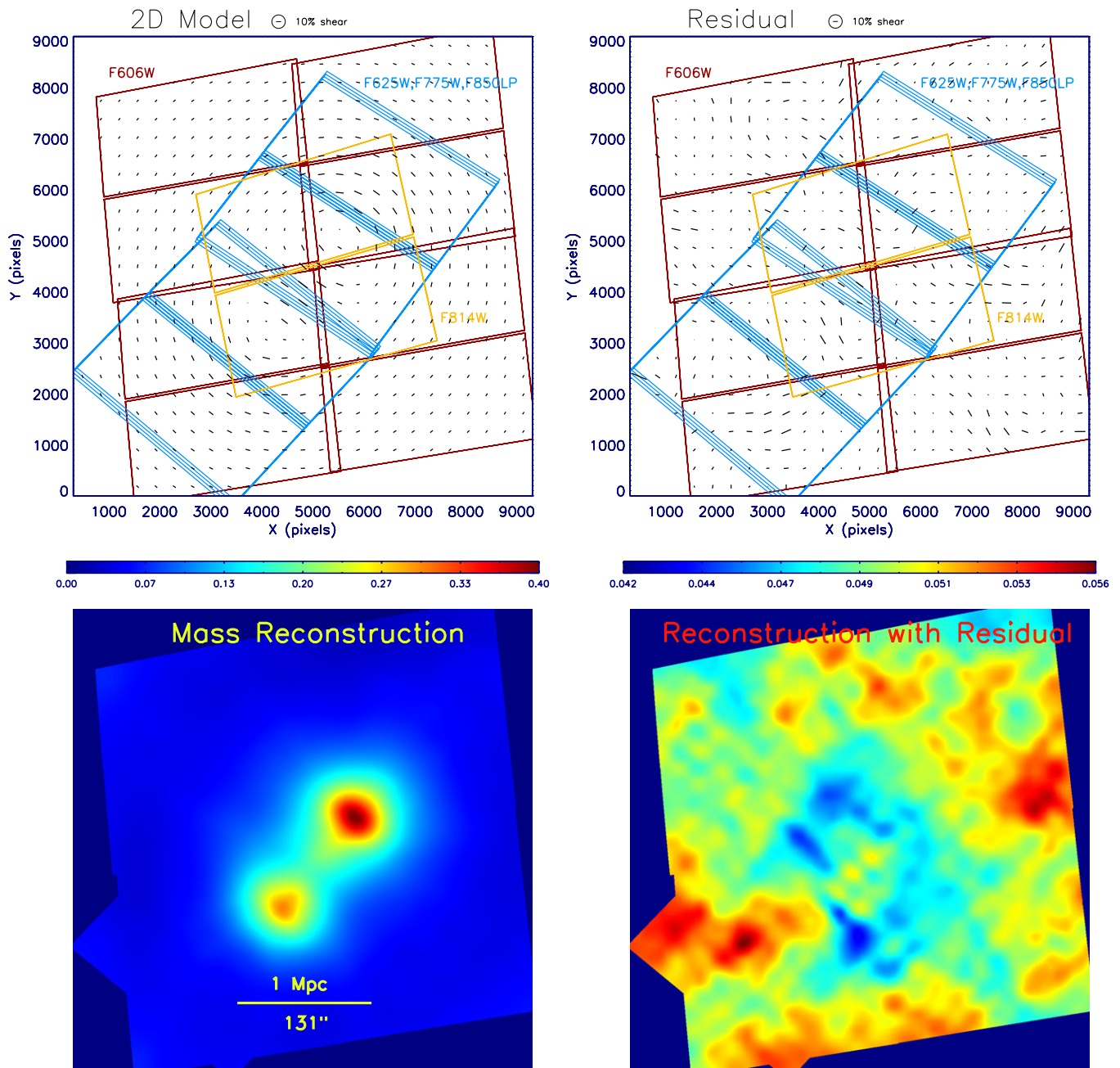
As mentioned above, the difference between our 2D and 1D results is small. Considering the potential sources of bias in the 1D analysis discussed above, we note that this small difference is interesting, although it is premature to draw any general conclusion from this single case. Because most weak-lensing studies in the literature do not use this 2D simultaneous fitting to constrain cluster masses (despite the fact that most clusters possess non-negligible substructures), it will be an important subject of future studies to examine the size and direction of the bias from a large sample.

Although we consider that our simultaneous 2D fitting procedure is the better method for cluster mass estimation given the small field size, the accuracy of the mass estimate depends on the degree that the real cluster mass distribution resembles our parametric description of it. To assess the validity of our assumption, we create a mock galaxy catalog based on our best-fit model and compare the result with the source catalog obtained from our *HST* images. The predicted ellipticity pattern is displayed in the upper-left panel of Figure 10. Also shown is the resulting convergence field (lower-left panel). The overall patterns in the ellipticity and convergence distributions are similar to those seen in our data (Figure 5). In particular, the ratio of the significance between the two mass peaks and their individual centroids are in good agreement. Detailed comparison is possible when their residuals (model-data) are plotted (right panels in Figure 10). The residual convergence (lower-right) is created from the residual ellipticities (not by subtracting two convergence fields) using the same maximum entropy method. The residuals can be attributed to correlated/uncorrelated large scale structure, departure from the axisymmetric NFW profile, and/or shape noise. Because of the mass-sheet ambiguity, the absolute convergence values are meaningless. Instead, one should pay attention to the range of the variation. The pick-to-valley variation is ∼0.01, which is smaller than our mass reconstruction rms values (Figure 6). The most significant residual is found in the SE region. This feature coinciding with a galaxy overdensity is also seen in our original mass reconstruction when a smaller smoothing scale is used. Nevertheless, there is no associated X-ray emission. It is not clear at the moment whether or not the structure is associated with ACT-CL J0102−4915. However, if we assume that this structure is at the cluster redshift, its mass from within an aperture of $r \sim 50''$ (∼380 h_{70}^{-1} kpc) is $\lesssim 1 \times 10^{14} h_{70}^{-1} M_\odot$. Therefore, we do not regard this extra substructure as a serious concern in our modeling of ACT-CL J0102−4915 with two massive NFW halos.

An alternative method to assess how well the 2D halo model describes the data is to examine the tangential shear values constructed from the residual ellipticity catalog. Figure 11 displays such test results azimuthally averaged around three different centers: the NW subcluster, the SE subcluster, and the global center. The residual signal is consistent with zero without any apparent large scale correlations.

It is important to examine how the two cluster masses are correlated in this full 2D analysis. A potential problem is that the two cluster masses might be highly anti-correlated. In other words, it may be possible that the fit would allow the two halos to trade mass with each other nonnegligibly while the χ^2 value remains relatively unchanged. Our MCMC analysis shows that

Figure 10. Two-dimensional mass modeling of ACT-CL J0102−4915. In the upper-left panel, we use our best-fit 2D NFW-fit results to display the predicted (noiseless) ellipticity of background galaxies and the resulting convergence. The upper-right panel displays the residuals, which can be attributed to the (correlated or uncorrelated) large scale structure, departures from the axisymmetric NFW profile, and/or simply shape noise. The corresponding convergence maps are shown in the bottom panels. Because of the mass-sheet ambiguity, the absolute convergence values are meaningless. Instead, one should pay attention to the range of the variation. The pick-to-valley variation is ∼0.01. The most significant residual is found in the SE region. This feature is also seen in our original mass reconstruction and coincides with a galaxy overdensity.

(A color version of this figure is available in the online journal.)

the degeneracy among fitted values, if any, is very weak as shown in Figure 12. We suspect that we do not suffer from this potential degeneracy because the mass estimates are mostly influenced by the *strong* weak-lensing signals at small radii ($r \lesssim 70''$) from each cluster's center. This also may explain why the masses obtained from the previous 1D analysis are similar to the current full 2D results. In Figure 13, we display the centroid distributions of the two halos, which illustrate that the mass centroid is well-constrained ($\lesssim 3''$).

As mentioned above, one of the most interesting issues concerning ACT-CL J0102−4915 is whether or not its total

mass lies sufficiently above a critical threshold that the cluster's mere existence gives rise to some non-negligible tension with theoretical predictions. As we use the mass function of Tinker et al. (2008) who choose M_{200c} or M_{200a} as a reference, we need to combine the masses of the two halos of ACT-CL J0102−4915 to estimate the equivalent quantity within a spherical volume. We implement the computation by populating a three-dimensional (3D; 1000^3) grid with the sum of the density distributions of the two halos. Figure 14 displays, as a function of radius, the resulting mass profile of the two individual halos of ACT-CL J0102−4915 (thick dotted and

Table 1
Mass Estimates of ACT-CL J0102−4915 Based on 1D Fit

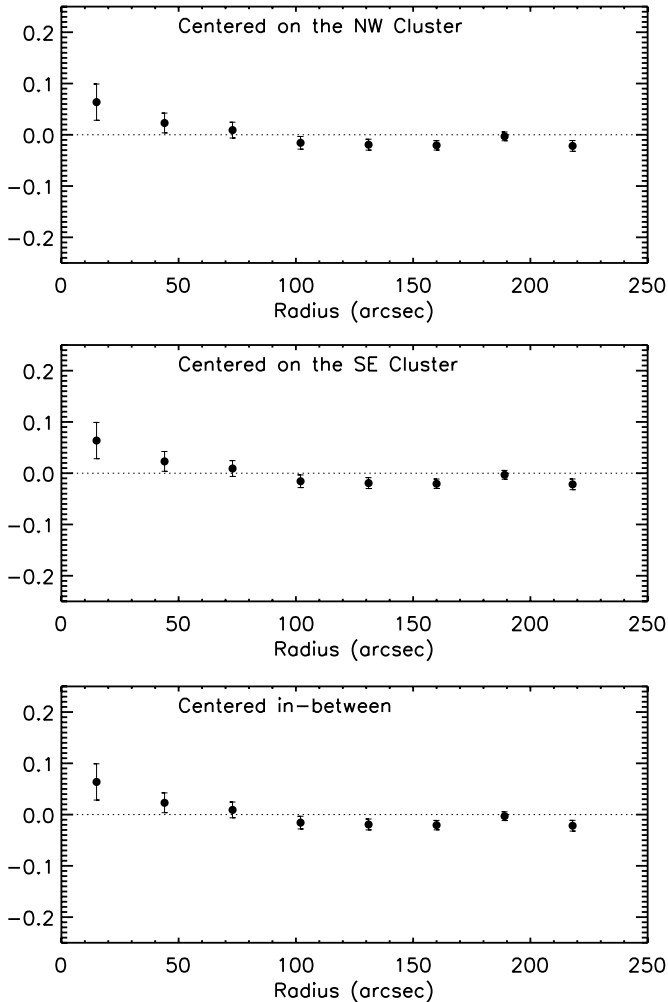| Clusters	σ_v (km s^{-1})	c_{200c}	R_{500c} (h_{70}^{-1} Mpc)	M_{500c} ($h_{70}^{-1} 10^{14} M_\odot$)	R_{200c} (h_{70}^{-1} Mpc)	M_{200c} ($h_{70}^{-1} 10^{14} M_\odot$)
NW	1129^{+46}_{-48}	2.57 ± 0.03	0.60 ± 0.03	4.00 ± 0.54	1.57 ± 0.08	11.7 ± 1.7
SE	1018^{+51}_{-54}	2.65 ± 0.04	0.53 ± 0.03	2.76 ± 0.49	1.38 ± 0.08	7.9 ± 1.4
Global[a]	1347^{+58}_{-60}	2.50 ± 0.03	0.66 ± 0.03	5.30 ± 0.08	1.74 ± 0.09	15.9 ± 2.4
NW+SE[b]	$\cdots$	$\cdots$	1.31 ± 0.06	16.8 ± 3.2	2.02 ± 0.16	25.4 ± 4.9

Notes.
[a] We assume that there is a single halo centered on the middle point of the NW and SE subclusters. The result is obtained from the outer ($>100''$) part of the tangential shears.
[b] We sum the masses of the NW and SE subclusters obtained from the individual tangential shear fitting results.

Table 2
Mass Estimates of ACT-CL J0102−4915 Based on Simultaneous 2D Fit

Clusters	σ_v (km s^{-1})	c_{200c}	R_{500c} (h_{70}^{-1} Mpc)	M_{500c} ($h_{70}^{-1} 10^{14} M_\odot$)	R_{200c} (h_{70}^{-1} Mpc)	M_{200c} ($h_{70}^{-1} 10^{14} M_\odot$)
NW	1133^{+58}_{-61}	2.54 ± 0.04	0.63 ± 0.03	4.58 ± 0.71	1.65 ± 0.10	13.8 ± 2.2
SE	1064^{+62}_{-66}	2.66 ± 0.06	0.53 ± 0.03	3.39 ± 0.56	1.37 ± 0.11	7.8 ± 2.0
NW+SE	$\cdots$	$\cdots$	1.34 ± 0.07	18.0 ± 3.4	2.09 ± 0.19	27.6 ± 5.1

Figure 11. Residual tangential shear profile. Shear values are estimated at the location of every source galaxy based on our best-fit 2D model, and these predicted shears are subtracted from the measured ellipticity. Then, the tangential shears are computed as done in Figure 9. Regardless of the choice of the center, the residual signal is consistent with zero. We omit the null (45° rotation) test to avoid cluttering the figure, but the level of scatter is comparable to the residual tangential shear values shown here.
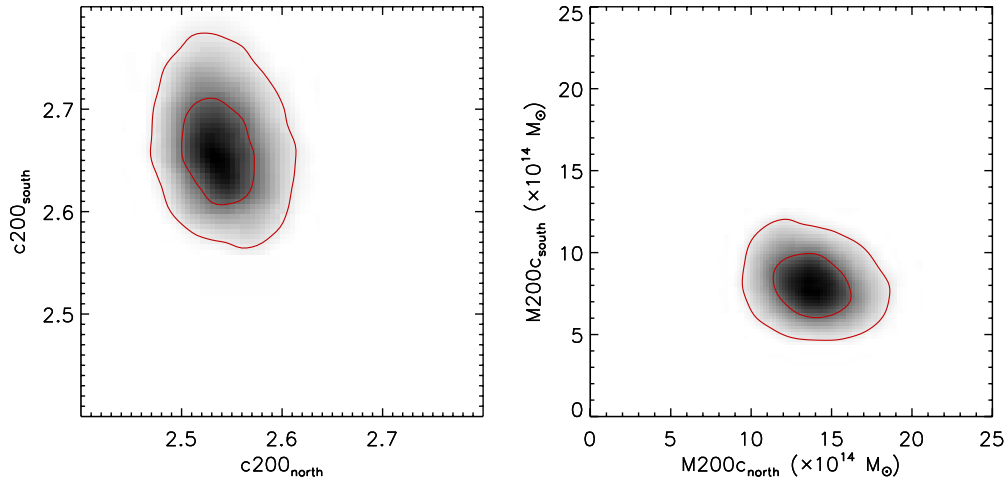
thick dashed lines) and the combined total (thick solid line). The thin solid and dashed lines represent the integrated total mass within a spherical volume of given radius for density values of 200 times the mean and critical densities of the universe at the cluster redshift, respectively. This allows the M_{200c} and M_{200a} values for the cluster to be conveniently determined by locating where the thin and thick lines intersect. The mass uncertainties of individual halos are about ∼18% at $r = 1.5 \, h_{70}^{-1}$ Mpc. Figure 14 shows that extrapolation of the two NFW halos to a radius of $r = 2.4 \, h_{70}^{-1}$ Mpc yields a combined mass of $M_{200a} = (3.13 \pm 0.56) \times 10^{15} \, h_{70}^{-1} \, M_\odot$.

The above mass estimation assumes that the two halos are at the same distance from us. This, of course, leads to a maximum value for the total mass. Here we investigate how much the combined mass decreases as we allow the two halos to have slightly different distances. We repeat the above total mass estimation, only now we populate the 3D grid while varying the angle between the merger axis (the line connecting the mass peaks) and the plane of the sky from zero to 80°. Figure 15 reveals that in fact the total mass of the system is not sensitive to the viewing angle as long as the angle is less than ∼65°, which would inflate the projected distance of ∼700 h_{70}^{-1} kpc to a physical separation of ∼2 h_{70}^{-1} Mpc.

M12 report that the line-of-sight velocity difference between the NW and SE components is 586 ± 96 km s^{-1}. This small relative velocity favors a scenario wherein the merger is happening nearly in the plane of the sky as long as the transverse velocity is sufficiently large (>1000 km s^{-1}. The presence of double radio relics in ACT-CL J0102−4915 (Lindner et al. 2013) also suggests that the merger axis is close to the plane of the sky. Unfortunately, no study has yet provided a secure constraint on the transverse velocity or 3D geometry of the merger.
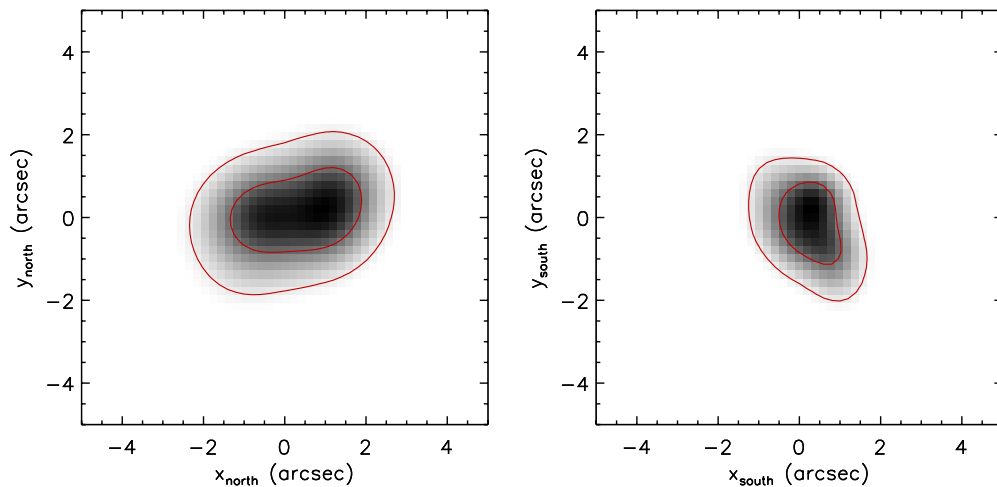
4.4. Mass Estimation Uncertainties from Various Sources

The mass estimate uncertainties presented in Section 4.3 include only shape noise arising from the finite number of source galaxies. Additional sources of uncertainty include the scatter in the mass–concentration relation, possible triaxiality of the halo,

Figure 12. Concentration and Virial Mass of ACT-CL J0102−4915. The results are obtained from our 80,000 MCMC samples by treating the cluster as a sum of two NFW halos. We show 1σ and 2σ contours. The mass–concentration relation of Duffy et al. (2008) is used, and thus if we know the result in one panel, the one in the other is determined.
(A color version of this figure is available in the online journal.)

Figure 13. Centroid distribution obtained from our 80,000 MCMC samples. We show 1σ and 2σ contours. We model ACT-CL J0102−4915 as a superposition of two NFW halos. Flat priors are assumed for the centroids with no boundary constraint. The results are displayed in the observed orientation (i.e., the same as in Figure 5).
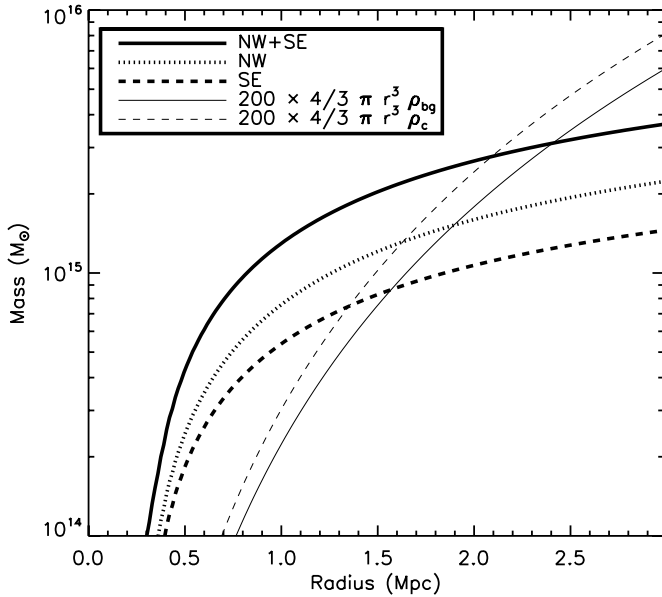(A color version of this figure is available in the online journal.)

and shear contribution from correlated/uncorrelated large-scale structures (LSSs).

Scatter in mass–concentration relation. The Duffy et al. (2008) mass–concentration relation possesses large scatter. Because we assume the mean relation to estimate the cluster mass, it is worth examining how much the mass estimate changes when we consider this scatter. Unfortunately, there are no large ($M_{200c} > 10^{14} M_\odot$) halos at $z \simeq 1$ in the numerical simulation of Duffy et al. (2008). Thus, the mass–concentration relation that we adopt is in fact an extrapolation from the results obtained for the $M_{200c} < 10^{14} M_\odot$ halos. In order to assess the impact of the mass–concentration uncertainty, we fit the one-parameter NFW profile while perturbing the concentration parameter around its mean by $\delta c_{200} = 0.5$ (the approximate scatter at $M_{200c} \sim 10^{14} M_\odot$ in the simulations). We find that the cluster mass changes by $\sim 10\%$ due to this effect.

Triaxiality, Large Scale Structure, and departure from NFW. Because our halo mass estimation inevitably assumes spherical symmetry, the deprojected mass estimate can be over/under-estimated depending on the actual degree and orientation of the triaxiality of ACT-CL J0102−4915. The masses of halos whose major axes are aligned along the line of sight are over-estimated whereas underestimation will occur when the major axes are perpendicular to the line of sight. Adding to this complexity are departure of the cluster mass profile from the NFW assumption and the LSSs along the line of sight. It is straightforward to quantify the scatter due to these sources using numerical simulations (e.g., Meneghetti et al. 2010; Becker & Kravtsov 2011; Oguri & Hamana 2011). According to Becker & Kravtsov (2011) who investigate the weak-lensing mass scatter from fitting an NFW profile to the shear profile, the intrinsic scatter is $\sim 20\%$ for massive halos and increases to $\sim 30\%$ for groups. Because the contribution from uncorrelated LSSs is about the same regardless of the halo mass, more massive clusters are less affected by LSSs. As each component of ACT-CL J0102−4915 is a massive system, it is legitimate to assume that the corresponding scatter (for each halo) may be $\sim 20\%$. While fitting an NFW model, Becker & Kravtsov (2011) varied both total mass and concentration independently. Therefore, the aforementioned scatter in the mass–concentration relation is already included in this estimation of the scatter.

Figure 14. Mass profile of ACT-CL J0102−4915. We use the results from simultaneous 2D fits of two NFW profiles. The thick dashed and dotted lines represent the masses within spherical volumes for individual halos whereas the thick solid line shows the sum of the two halos assuming that the projected distance is the actual physical separation (we choose the center of mass of the two halos for the origin). The thin solid and dashed lines represent the total mass enclosed within the sphere at r when the density inside becomes 200 times the mean and critical densities of the universe at the cluster redshift, respectively. The M_{200c} and M_{200a} values are easily determined by locating where the thin and thick lines intersect. The statistical uncertainties of individual masses are about ∼20% at $r = 1.5 \, h_{70}^{-1}$ Mpc.
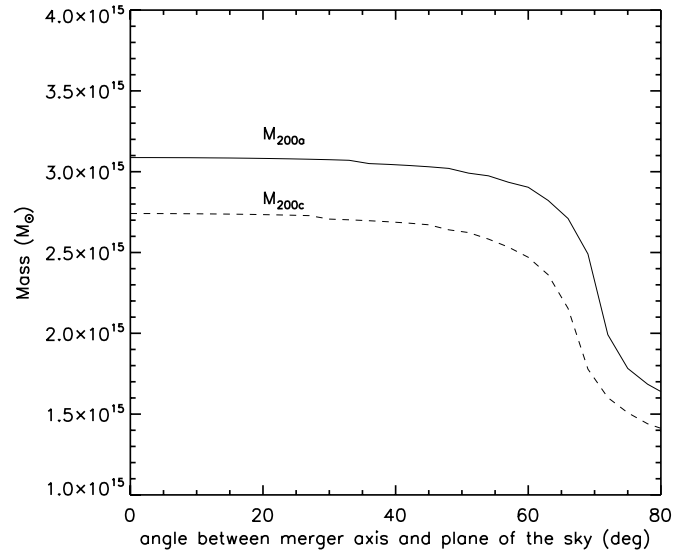
4.5. Luminosity Estimation and Mass-to-Light Ratio

High mass-to-light ratio (M/L) values for galaxy clusters have been firmly established today and provide critical evidence for the dominance of dark matter in the large-scale structure of the universe. Studies of cluster M/L values in a broad range of environments provide key information for us to understand the formation of clusters and their member galaxies. ACT-CL J0102−4915 distinguishes itself from other clusters by its extremely high mass despite being at high redshift. Thus, an investigation of the M/L values of this unusual cluster is an important extension of the environmental baseline in cluster M/L studies.

We define two maximally non-overlapping circular apertures each with a radius of $r = 386 \, h_{70}^{-1}$ kpc (i.e., half the projected distance between the NW and SE clumps) centered on the luminosity peaks. The cluster galaxies are identified by combining our spectroscopic survey data (Sifón et al. 2013) and photometric redshift catalog (M12). The rest-frame B-band at $z = 0.87$ overlaps both the F775W and F850LP filter throughput curves. We choose to use the *HST*/ACS photometry to estimate the rest-frame B-band luminosity of ACT-CL J0102−4915 via the following relation:

$$B_{\rm rest} = -0.565({\rm F775W} - {\rm F850LP}) + 1.38 - {\rm DM}, \quad (11)$$

where DM is the distance modulus at the cluster redshift. The above relation is derived from our synthetic photometry using the Kinney et al. (1996) spectral energy distribution template.

The column mass within the aperture is computed using both the best-fit NFW parameters and aperture-mass densitometry (Fahlman et al. 1994). Readers are referred to Bartelmann

Figure 15. Total cluster mass as a function of viewing angle. The sum of the two halos in ACT-CL J0102−4915 weakly depends on the viewing angle as shown here. The total cluster mass remains extremely high until we assume that angle between the merger axis and the plane of the sky becomes greater than ∼65°, in which case the separation between the two halos is more than ∼2.3 h_{70}^{-1} Mpc.

(1996) for the useful equations for the computation of the NFW profile column density. The best-fit NFW parameters (from the 2D fit method) give $(4.20 \pm 0.34) \times 10^{14} \, h_{70}^{-1} \, M_\odot$ and $(2.98 \pm 0.25) \times 10^{14} \, h_{70}^{-1} \, M_\odot$ for the NW and SE clusters, respectively, within the $r = 386 \, h_{70}^{-1}$ kpc aperture. The NFW-fitting results for both NW and SE are consistent with the values from the aperture densitometry, which gives $(3.92 \pm 0.36) \times 10^{14} \, h_{70}^{-1} \, M_\odot$ and $(3.42 \pm 0.31) \times 10^{14} \, h_{70}^{-1} \, M_\odot$, respectively. Aperture densitometry requires us to define a control annulus, and we use the $r = 1–1.5 \, h_{70}^{-1}$ Mpc region for each cluster. We derive the mean column density within the annulus using the best-fit NFW parameters, taking into account the two overlapping profiles. The mean surface mass densities for the NW and SE annuli are estimated to be $\bar{\kappa} = 0.067$ and 0.065, respectively. Note that since these values are non-negligibly higher than zero, our estimates based on the aperture mass densitometry are not entirely independent of our parametric estimation.

We summarize the M/L values of ACT-CL J0102−4915 in Table 3. Our analysis shows that the M/L value of the NW subcluster ($\sim 130 \, h_{70} \, M_\odot / L_{B\odot}$) is higher than that ($\sim 88 \, h_{70} \, M_\odot / L_{B\odot}$) of the SE subcluster (25%–50% depending on the method). Comparison of this M/L value with those of other clusters requires caution because the radial variation of the M/L ratio is cluster-dependent. For example, the cumulative M/L profile of Cl0152−1357 at $z = 0.83$ rises steeply at small radii, peaking at $\sim 270 \, h_{70}^{-1}$ kpc with $M/L \sim 150 \, h_{70} \, M_\odot / L_{B\odot}$. At larger radii, the M/L value gradually decreases and reaches $\sim 95 \, h_{70} \, M_\odot / L_{B\odot}$ at $r = 1 \, h_{70}^{-1}$ Mpc (Jee et al. 2005a). On the other hand, the cumulative M/L profile of MS1054−0321 at a similar redshift of $z = 0.83$ continues to increase with radius, reaching $\sim 120 \, h_{70} \, M_\odot / L_{B\odot}$ at $r = 1 \, h_{70}^{-1}$ Mpc (Jee et al. 2005b). Within the $r = 386 \, h_{70}^{-1}$ kpc aperture the difference between the two $z \sim 0.83$ clusters' M/L values is non-negligible ($\sim 140 \, h_{70} \, M_\odot / L_{B\odot}$ and $\sim 90 \, h_{70} \, M_\odot / L_{B\odot}$ for Cl0152−1357 and MS1054−0321, respectively). With this caveat in mind,

Table 3
Luminosity and Mass-to-Light Ratio of ACT-CL J0102−4915

	NW Subcluster	SE Subcluster
B-band luminosity	$3.22 \times 10^{12} \, h_{70}^{-2} \, L_{B\odot}$	$3.40 \times 10^{12} \, h_{70}^{-2} \, L_{B\odot}$
Column mass ($r < 386 \, h_{70}^{-1}$ kpc)	$4.20 \pm 0.34 \, (3.92 \pm 0.36) \times 10^{14} \, h_{70}^{-1} \, M_{\odot}$	$2.98 \pm 0.25 \, (3.42 \pm 0.31) \times 10^{14} \, h_{70}^{-1} \, M_{\odot}$
Mass-to-light ratio	$130 \pm 10 \, (122 \pm 11) \, h_{70} \, M_{\odot}/L_{B\odot}$	$88 \pm 7 \, (101 \pm 9) \, h_{70} \, M_{\odot}/L_{B\odot}$

Note. [a] The numbers in parentheses are derived from aperture mass densitometry.

we conclude that the M/L value of ACT-CL J0102−4915 is well-bracketed by the M/L values of these two clusters.
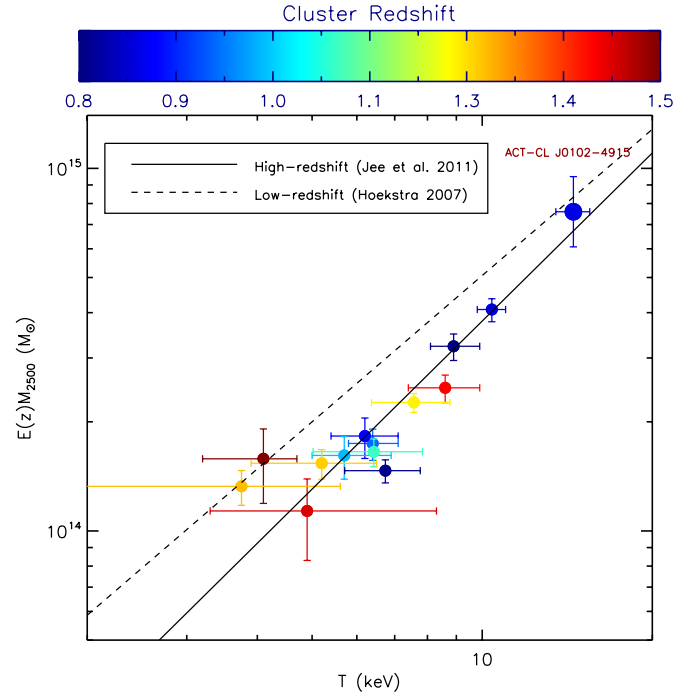
5. DISCUSSION

5.1. Comparison with Other Observations

ACT-CL J0102−4915 was first discovered by ACT as the cluster with their survey's most significant SZ decrement and an X-ray luminosity comparable to that of the Bullet Cluster (Marriage et al. 2011). Using their own mass scaling relation, Williamson et al. (2011) estimated $M_{200a} = (1.89 \pm 0.45) \times 10^{15} \, h_{70}^{-1} \, M_{\odot}$ from the SPT data.

More robust mass estimates of ACT-CL J0102−4915 were presented by M12, who performed a joint analysis of the *Chandra* X-ray, ACT SZ, and dynamical data and quoted $M_{200a} = (2.16 \pm 0.32) \times 10^{15} \, h_{70}^{-1} \, M_{\odot}$. This value is statistically consistent with the result of Williamson et al. (2011).

However, it is noteworthy that the M12 mass estimates based on individual scaling relations show large variations. For example, the M_{500c}–$M_{\rm gas}$ scaling relation predicts $M_{200a} \sim 3.1 \times 10^{15} \, h_{70}^{-1} \, M_{\odot}$ whereas the dynamical relation (M_{200a}–σ) gives $M_{200a} \sim 1.86 \times 10^{15} \, h_{70}^{-1} \, M_{\odot}$, a factor of 1.7 times smaller than the former.

Our total mass estimate from the current weak-lensing study $M_{200a} = (3.13 \pm 0.56) \times 10^{15} \, h_{70}^{-1} \, M_{\odot}$ is fully consistent with the X-ray-based mass estimates of M12, including their value based on Y_X which is $M_{200a} = 2.88^{+0.78}_{-0.55} \times 10^{15} \, h_{70}^{-1} \, M_{\odot}$. We find that the discrepancy between the cluster's dynamical mass and the current weak-lensing mass can be reconciled if we treat the ACT-CL J0102−4915 system as two components. For example, the dynamical masses of the two individual subclusters ($M_{200a} = 1.76^{+0.62}_{-0.58} \times 10^{15} \, h_{70}^{-1} \, M_{\odot}$ and $1.06^{+0.64}_{-0.59} \times 10^{15} \, h_{70}^{-1} \, M_{\odot}$ for the NW and SE subclusters, respectively) estimated by M12 are consistent with our lensing results (also, remember that the lensing-based velocity dispersion estimates are in good agreement with the spectroscopic measurements). M12 quote a total mass of the system $M_{200a} = 1.86^{+0.54}_{-0.49} \times 10^{15} \, h_{70}^{-1} \, M_{\odot}$ based on the combined total velocity dispersion of $\sim$1321 km s^{-1}, which is only $\sim$6% higher than their mass of the NW cluster. Instead, if we regard ACT-CL J0102−4915 as two components with each following the Duffy et al. (2008) mass–concentration relation, the combination of the two dynamical masses of M12 will yield $M_{200a} = (3.8 \pm 0.8) \times 10^{15} \, h_{70}^{-1} \, M_{\odot}$ consistent with our lensing estimate. Note that combining the two halos increases r_{200a}, which makes the total M_{200a} greater than the sum of the two individual components' M_{200a} values. We further note that the dynamical mass estimates are based on measurements of the radial velocities of cluster member galaxies. If the axis of the two infalling subclusters is close to the plane of the sky, then there would be a significant component of kinetic energy that is not yet virialized and which would not be included in the total combined velocity dispersion measurement.

Figure 16. Mass vs. temperature relation of ACT-CL J0102−4915. The data points except for ACT-CL J0102−4915 display the weak-lensing masses and X-ray temperatures of the 13 high-redshift ($z \gtrsim 0.8$) clusters presented in Jee et al. (2011). The solid line shows a best-fit result to these 13 data points ($M \propto T^{1.54}$). The dashed line ($M \propto T^{1.34}$) represents the low-redshift result from Hoekstra (2007). The two slopes are statistically consistent whereas the normalization (i.e., translation) is different at the $>3\sigma$ level. Jee et al. (2011) interpret the difference as indicating a possible evolution of the normalization in the M–T_X relation. We compute M_{2500} of ACT-CL J0102−4915 by defining a fictitious single NFW halo that yields $M_{200c} = 2.75^{+0.74}_{-0.59} \times 10^{15} \, h_{70}^{-1} \, M_{\odot}$.
(A color version of this figure is available in the online journal.)

Having shown consistency between the weak-lensing and X-ray-derived masses, we now compare the X-ray temperature versus weak-lensing mass relation of ACT-CL J0102−4915 with those of other high-redshift clusters. Previous mass–temperature relation studies quote cluster masses in M_{2500c}, which refers to the mass within a smaller radius r_{2500c} than the typical virial radius r_{200a}. Thus, unlike M_{200a}, M_{2500c} is sensitive to the choice of the cluster center in ACT-CL J0102−4915 because the shape of the combined halos are "peanut-like." Therefore, we define a single cluster whose virial mass matches the total cluster mass $M_{200c} = (2.76 \pm 0.51) \times 10^{15} \, h_{70}^{-1} \, M_{\odot}$ (Table 2). The corresponding NFW parameters are obtained from the Duffy et al. (2008) relation. As shown in Figure 16, ACT-CL J0102−4915 follows the M–T_X relation of other galaxy clusters.

The weak-lensing, X-ray, and dynamical studies consistently support the extreme mass of ACT-CL J0102−4915, projecting the system to be the most massive cluster at $z > 0.6$. However,

we find that the SZ mass $1.64^{+0.62}_{-0.42} \times 10^{15} h_{70}^{-1} M_\odot$ of M12 is significantly lower than the other measurements, indicating that perhaps more efforts are needed to calibrate the SZ mass proxy yT_{CMB}.

Zitrin et al. (2013) present a strong-lensing analysis of ACT-CL J0102−4915 and provide a rough mass estimate of $M_{200c} \simeq 2.3 \times 10^{15} h_{70}^{-1} M_\odot$ for the entire system. This total mass estimate roughly corresponds to the 1σ lower limit of the current weak-lensing result. Since the strong-lensing analysis of Zitrin et al. (2013) is based on poorly constrained three band *HST*/ACS photometric redshifts, no significant constraint on the slope of the mass profile is provided. Therefore, a detailed discussion on the discrepancy in the total mass estimation by weak and strong lensing should be deferred until secure spectroscopic redshifts are obtained for the multiply-lensed background galaxies. However, it is still worthwhile to mention one discrepancy in the mass ratio of the two subclusters between the current weak-lensing study and the strong-lensing analysis. The Zitrin et al. (2013) strong-lensing model suggests that the SE clump is more massive than the NW one by a factor of 1.5 whereas our weak-lensing analysis indicates that the NW cluster is nearly twice as massive as the SE cluster, which is supported by the peak intensity in mass reconstruction, the 2D ellipticity distribution (i.e., whisker plot), and the 1D tangential shear profiles.

This issue of the mass ratio between the two subcluster components is important when one attempts to model the system with numerical simulations because the mass ratio is pivotal in determining many of the observed features including the likelihood of the survival of gas peaks, the temperature structure, the morphology/direction of the wake, and so on.

5.2. Is ACT-CL J0102−4915 a High-redshift Analog of the Bullet Cluster?

Comparison of ACT-CL J0102−4915 to the Bullet Cluster is first mentioned in Marriage et al. (2011), however, only in the context of discussing the significance of the overall SZ decrement. M12 suggest that ACT-CL J0102−4915 might be a high-redshift analog of the Bullet Cluster also as regards its stage of merger. They find that (1) the peak of the X-ray emission is the coolest region, (2) the Fe abundance of the X-ray peak is significantly enhanced, (3) the temperature structure is indicative of shock heating, (4) the X-ray surface brightness falls off steeply beyond the SE subcluster, (5) there is a wake toward the NW subcluster, (6) the radio data indicate the possible presence of an intense double radio relic (now confirmed by Lindner et al. 2013), and (7) the SE galaxy distribution is offset to the southeast with respect to the X-ray peak. M12 interpret these lines of evidence as indicating that the cool X-ray peak is moving southeast after passing through the core of the other subcluster.

However, there is one major difference in the X-ray morphology between the Bullet Cluster and ACT-CL J0102−4915. In the Bullet Cluster, there are two distinct X-ray surface brightness peaks that can be associated with the main cluster and the subcluster. In contrast, the *Chandra* X-ray map of ACT-CL J0102−4915 shows only a single X-ray peak located close to the SE mass peak. Although the X-ray emission is extended from this peak to the NW component, we cannot identify any distinct second X-ray peak in this region. This difference could be attributed to the different mass ratio of its components ($\sim$2:1) compared to that of the Bullet Cluster ($\sim$10:1). It looks like the interaction in ACT-CL J0102−4915 has mostly

disrupted the central gas core initially present in the NW component. This scenario is supported by the presence of a strong wake in the SE–NW direction to the NW of the X-ray peak.

As in the case of the Bullet Cluster, there is an offset between the gas and weak-lensing mass peaks in ACT-CL J0102−4915, although the separation in the Bullet Cluster is larger ($d \sim 150 \, h_{70}^{-1}$ kpc) than in ACT-CL J0102−4915 ($d \sim 100 \, h_{70}^{-1}$ kpc). The statistical significance of the position offset between the gas and weak-lensing mass peaks is a strong lower limit on the significance of the position offset between the gas and dark matter peaks. Since a non-negligible fraction of the total mass at the location of the X-ray peak is contributed by the gas itself, if we were to remove the baryonic mass from the weak-lensing mass distribution, the pure dark matter peak would move to the west in ACT-CL J0102−4915, further from the gas peak. To make this correction and remove the cluster gas mass from the weak-lensing mass reconstruction requires a careful analysis of the X-ray data, which is underway and will be the focus of an upcoming study

In the Bullet Cluster the X-ray peaks are trailing the corresponding mass peaks if we assume that the two components are moving apart from each other. The direction of the offset is consistent with the hypothesis that dark matter particles are collisionless whereas the cluster plasma is subject to ram pressure. However, in ACT-CL J0102−4915 the gas peak is leading the mass peak if we assume a similar stage of the merger. We have considered two possible scenarios for the merger in ACT-CL J0102−4915: (1) we are viewing after core passage, but before first turn around, and the merger speed is low or (2) the merger speed is high, but we are viewing after the first turnaround as the two components come together for a second core passage. In the first case the ρv^2 gas pressure that tends to cause the dark matter-gas disassociation in the Bullet Cluster is negligible (or much less) in ACT-CL J0102−4915 and we would expect that the gas and dark matter should not be significantly disassociated. For the second case we view the dark matter as moving more freely than the gas, preceding it after first core passage (as seen in the Bullet Cluster) and then, being less encumbered than the gas, returning more quickly back toward a second encounter with the NW component. Whether or not the dark matter can overtake and pass the gas component on its second inward core passage (as we seem to require in ACT-CL J0102−4915) remains to be studied with *n*-body and hydrodynamical simulations of the merger.

5.3. How Rare is a Massive Cluster Like ACT-CL J0102−4915?

Recent discoveries of extremely massive high-redshift clusters (e.g., Brodwin et al. 2012; Stanford et al. 2012; Jee et al. 2009; Foley et al. 2011; Menanteau et al. 2012; Planck Collaboration et al. 2011) kindled the debate over the consistency of the existence of these massive clusters with the current ΛCDM paradigm (e.g., Cayón et al. 2011; Jimenez & Verde 2009; Gonzalez et al. 2012; Hoyle et al. 2011; Meneghetti et al. 2011; Mortonson et al. 2011; Waizmann et al. 2012; Harrison & Coles 2012; Hotchkiss 2011). At the heart of this debate is the proper estimation of the survey volumes and their selection functions that led to those discoveries.

Conservative studies tend to use the entire existing cluster surveys or the full sky area as a reference to estimate the probabilities whereas others on the opposite extreme consider only the selection function of the parent survey for their abundance estimation. Moreover, some conservative studies

claim that the minimum redshift that one uses for the survey volume estimation should be significantly lower than the redshift of the cluster in question (e.g., Hotchkiss 2011).

M12 concluded that although ACT-CL J0102−4915 is an extremely rare system, the presence of the cluster is still consistent with the standard ΛCDM cosmology in the lower part of its allowed mass range. In this paper, we revisit the question with the current weak-lensing mass estimate.

Because ACT-CL J0102−4915 consists of two components, an important question is whether or not it is legitimate to treat it as a single system when its rarity is investigated. A critical parameter to be considered is the viewing angle with respect to the merger axis. In Section 4.3, we demonstrated that the total cluster mass remains high as long as the angle between the merger axis and the plane of the sky is less than ∼70°. However, at this angle, the physical separation of the two clusters becomes about $2\,h_{70}^{-1}$ Mpc, in which case cluster finding algorithms in N-body data (most popular mass functions are calibrated with N-body data) may identify them as two distinct clusters. Addressing exactly where the division happens is beyond the scope of the current study. In the following, our analysis assumes that the Tinker et al. (2008) mass function is still valid in estimating the abundance of a massive binary system such as ACT-CL J0102−4915.

A traditional method to test the possible tension between the existence of an extremely massive cluster and the given cosmology is to estimate the probability of the cluster discovery within the assumed cosmology. In a survey of the entire sky, the number of clusters with mass and redshift greater than M_{min} and z_{min}, respectively is given by

$$N(M,z) = \int_{z_{\mathrm{min}}}^{z_{\mathrm{max}}} \frac{dV(z)}{dz} dz \int_{M_{\mathrm{min}}}^{M_{\mathrm{max}}} \frac{dn}{dM} dM \qquad (12)$$
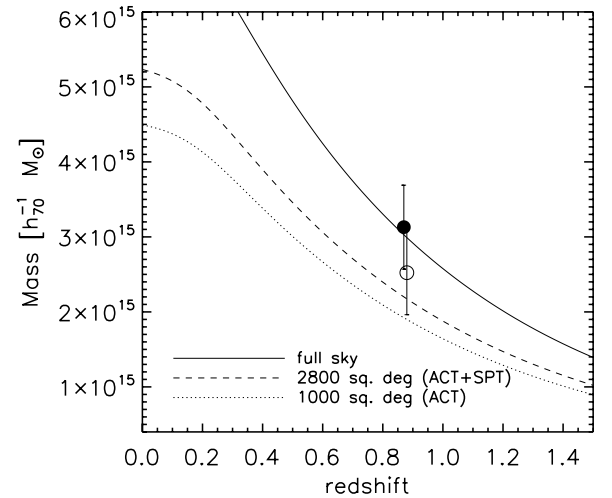
where dV/dz is the volume element and dn/dM is the mass function. For massive high-redshift clusters, the result is sensitive to the mass function dn/dM near z_{min} and M_{min}.

The choice of the threshold mass M_{min} is somewhat subjective. Mortonson et al. (2011) argue that an Eddington bias (Eddington 1913) is a non-negligible factor when the cosmological significance using most massive clusters is discussed. Although we include this factor when we perform the Mortonson et al. (2011) exclusion curve test below, our analysis with the traditional method is carried out without the consideration of the Eddington bias. Therefore, we use the statistical 1σ lower limit of $M_{200a} = (3.13 \pm 0.56) \times 10^{15}\,h_{70}^{-1}\,M_{\odot}$.

Similarly, the choice of the minimum redshift z_{min} is also a subject for debate. Equation (12) clearly ignores the case where a similarly rare cluster exists at a lower redshift with a higher mass (Hotchkiss 2011). In some surveys where one is preferentially looking for high-redshift clusters (e.g., archival data search), the issue is not critical. However, in relatively complete surveys, the negligence can lead to substantial bias in rarity estimation (Hotchkiss 2011).

Hotchkiss (2011) also discussed the case, where a similarly rare cluster exists at higher redshift but with a *lower mass* not included in Equation (12). However, considering the typical detection limit of the existing surveys, this bias should be small when the cluster redshift is sufficiently high ($z \sim 1$).

Assuming the cosmological parameters favored by the Wilkinson Microwave Anisotropy Probe 9 yr results (Bennett et al. 2013), we estimate that the expected number of clusters like ACT-CL J0102−4915 is ∼0.01 over the full sky. Because the existing SZ surveys (SPT+ACT) cover only ∼7% of the entire sky,

Figure 17. Exclusion curves and weak-lensing mass estimate of ACT-CL J0102−4915. We display 95% probability curves, which exclude both cosmological parameter and sample variances at the 95% level. The open and filled circles show our weak-lensing mass estimates with and without the application of the Eddington bias correction, respectively.

this full-sky assumption is conservative. Recent *Planck* cosmological parameter estimation studies (Planck collaboration et al. 2013b) favor slightly higher values in both matter density (Ω_M) and fluctuation on a 8 Mpc scale (σ_8), which increases the expected abundance of clusters like ACT-CL J0102−4915 nearly by a factor of five (i.e., probability of ∼0.05). This illustrates how sensitive the mass function of high-redshift clusters at the high end is to these two parameters.

Apart from the aforementioned ambiguity in choosing the lower limits of the integration, the above approach is inefficient for quantifying the impact of both cosmological parameter uncertainties and sample variance at the same time. In other words, the method does not address the case where the abundance of a massive cluster is not extremely low when the assumed cosmology is, for example, at the 2σ tail of the fiducial cosmology.

Mortonson et al. (2011) defined an "exclusion curve" that overcomes this pitfall. M12 compared the exclusion curve with their mass of ACT-CL J0102−4915 and showed that the central value of the cluster mass lies on the 95% exclusion curve for the combined ACT+SPT survey area (2800 deg²). Nevertheless, because of their mass uncertainties, they concluded that the presence of ACT-CL J0102−4915 does not give rise to any significant tension with the standard ΛCDM. We display the same Mortonson et al. (2011) 95% exclusion curves with the current weak-lensing mass estimate of ACT-CL J0102−4915 in Figure 17. The central value of ACT-CL J0102−4915 lies slightly above the 95% exclusion curve computed for the full sky, and its 1σ lower limit is above the existing SZ survey area.

As mentioned above, a more conservative approach uses Eddington bias to account for the asymmetric scatter probability for steep mass functions: namely that the chance of up-scatter is higher than that of down-scatter. We estimate the reduced mass M' using the Mortonson et al. (2011) prescription: $M' = \exp(1/2\gamma\sigma_{\ln M})M$, where γ is the local power-law slope ($dn/d\ln M \sim M^{\gamma}$), and $\sigma_{\ln M}$ is the 1σ uncertainty of $\ln M$ (log-normal distribution is assumed for mass errors). We also display this Eddington-bias-corrected mass value (open circle) in Figure 17, which shows that the 1σ lower limit of this reduced mass is slightly below the exclusion curve computed for the total ACT survey area (1000 deg²).

18

The uncertainties in Figure 17 show only the statistical uncertainties. As discussed in Section 4.4, the total mass uncertainty can be as large as $\sim$20% to $\sim$30% when we include the major systematic uncertainties such as triaxiality.

Harrison & Hotchkiss (2013) suggest some modifications to the Mortonson et al. (2011) exclusion curve in such a way that the exclusion curve includes the cases where similarly rare clusters might exist at lower (higher) redshift with higher (lower) masses. This modified exclusion curve gives a threshold mass approximately a factor of two higher than that of Mortonson et al. (2011) at the cluster redshift.

Therefore, despite the extremely high mass of ACT-CL J0102$-$4915 when the universe is half its current age, the above rarity test shows that the cluster by itself will not pose a significant challenge to the current ΛCDM model.

It is important to remember that our weak-lensing mass estimate M_{200a} is obtained by extrapolation. The current ACS field covers approximately a $\sim$2.75 h_{70}^{-1} Mpc $\times \sim$ 2.75 h_{70}^{-1} Mpc square region whereas r_{200a} for the entire system is $\sim$2.4 h_{70}^{-1} Mpc. Although currently there is no indication that the cluster mass density may fall off steeply outside the ACS field of view, a more robust M_{200a} mass estimation requires a much larger weak-lensing field.

In addition, our theoretical understanding of the mass function at the extreme end is incomplete. Extreme clusters such as ACT-CL J0102$-$4915 are rare even in the current largest cosmological simulations. Therefore, the use of the Tinker et al. (2008) mass function in the current study is an extrapolation.

6. CONCLUSIONS

We have presented a detailed weak-lensing analysis of ACT-CL J0102$-$4915 at $z = 0.87$, the most significant SZ decrement in the ACT and SPT surveys. Our analysis confirms that ACT-CL J0102$-$4915 consists of two massive components with a projected separation of $\sim$700 h_{70}^{-1} kpc. Our mass determination requires care because of the limited field of view in weak-lensing data and also this binary structure. We estimate the mass of ACT-CL J0102$-$4915 by simultaneously fitting two axisymmetric NFW profiles allowing their centers to vary. The masses of the NW and the SE components are $M_{200c} = (1.38 \pm 0.22) \times 10^{15} h_{70}^{-1} M_\odot$ and $(0.78 \pm 0.20) \times 10^{15} h_{70}^{-1} M_\odot$, respectively. These two lensing masses are consistent with the results from dynamical studies.

The small line-of-sight velocity difference between the NW and SE components ($\sim$600 km s^{-1}) and the presence of double radio relics suggests that the merger is proceeding nearly in the plane of the sky. With this plane-of-the-sky-merger hypothesis, extrapolation of the two NFW halos to a radius $r = 2.4 h_{70}^{-1}$ Mpc yields a combined mass of $M_{200a} = (3.13 \pm 0.56) \times 10^{15} h_{70}^{-1} M_\odot$, which is consistent with our two-component dynamical analysis and previous X-ray measurements.

At face value, the existence of such an extreme cluster may be viewed as a challenge to the current ΛCDM paradigm. However, such a claim awaits further studies addressing the validity of the extrapolation of the cluster mass profile beyond the current field size, as well as the extrapolation of the current empirical mass function calibrated with relatively low-volume N-body simulations.

ACT-CL J0102$-$4915 resembles the Bullet Cluster when it comes to its extreme mass and binary distribution of galaxies and dark matter. However, the X-ray map shows only a single distinct gas peak located close to the less massive SE subcluster. Although we detect an offset between the SE mass center and the X-ray peak, the mass peak does not seem to be leading the gas peak if we are viewing the cluster soon after first core passage during a high speed merger as in the Bullet Cluster.

APPENDIX A

IMPACTS OF CTI ON WEAK-LENSING ANALYSIS OF ACT-CL J0102$-$4915
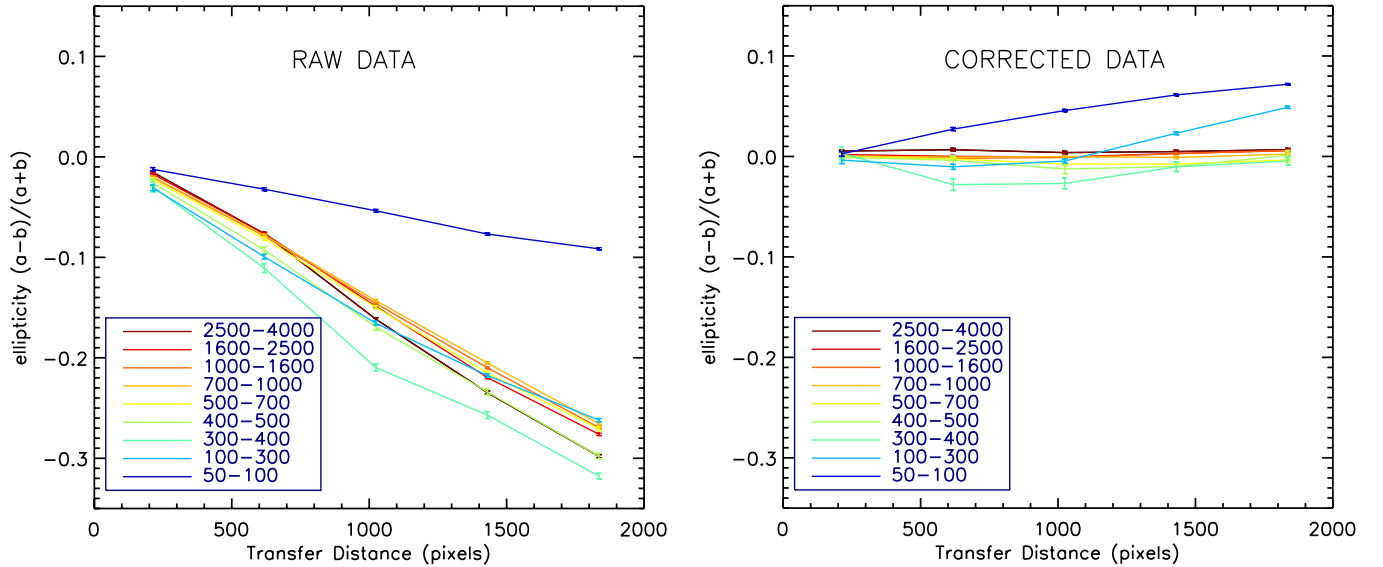
A.1. CTI Measurement

The current *HST*/ACS data of ACT-CL J0102$-$4915 was taken on 2012 September and October. This is more than three years since Servicing Mission 4 in 2009 May and more than 10 yr since the camera was installed in 2002 March. Cumulative damage on the CCDs due to space radiation is severe, and the resulting CTI is of great concern for the use of the ACS instrument in weak-lensing studies. Here we present our investigation of CTI and its impact on our weak-lensing using the PROP 12755 data.

Many techniques have been suggested to characterize CTI effects including differential aperture photometry, monitoring warm pixels and their trails, etc. In this paper, we measure the ACS CTI utilizing sub-seeing features (SSFs). We refer to any group of connected pixels whose size is less than that of the PSF, but whose collective significance is well above the sky rms as SSFs. Most SSFs are cosmic-rays or uncorrected hot/warm pixels. Because they are not affected by the PSF, their collective shapes are useful indicators of CTI trails.

In the left panel of Figure 18, we display the ellipticity of the SSFs detected on the current ACT-CL J0102$-$4915 *HST* images as a function of transfer distance. Because the analysis is performed on the FLT images (i.e., prior to geometric distortion correction), the parallel CTI happens purely along the readout direction. As observed, our definition of the y-axis being this readout direction makes the CTI-induced ellipticity negative. Two features of the ACS CTI are noteworthy. First, the CTI increases linearly with transfer distance, which is consistent with theoretical expectations and previous results. Second, no strong flux-dependence is seen except for the data with the lowest counts (50–100 e^{-1}). This behavior is different from what we obtain with earlier ACS images. For example, Figure 30 of Jee et al. (2011) shows that the CTI slopes measured from the year 2006 data set depend sensitively on flux.

The right panel of Figure 18 is the same as the left panel except that we repeat the measurement using the FLC images. These FLC images provided by the STScI pipeline are corrected for the CTI with the pixel-based method (Ubeda & Anderson 2012), and therefore the result reveals residual CTI effects on SSFs after the correction. The performance is remarkable for the bright (300–4000 e^{-1}) SSFs, as indicated by their residual ellipticities close to zero. For the faint SSFs (50–300 e^{-1}),

Figure 18. CTI effects on the ellipticity of sub-seeing features (SSFs). We measure the ellipticity of the SSFs (e.g., cosmic-rays) to characterize the CTI effect. We define the *x*-axis orthogonal to the readout direction, and thus the CTI-induced elongation gives a negative ellipticity. The curves of different color represent the SSFs of different flux ranges. The left panel shows the results obtained from the raw images of ACT-CL J0102−4915 whereas the right panel displays the measurements from images where the CTI effect has been corrected for by the STScI pipeline using the Ubeda & Anderson (2012) algorithm. The correction reduces the CTI effect substantially, although the residual errors are still non-negligible at the faint limit. Note the CTI over-correction in the 50–100 e$^-$ regime.

(A color version of this figure is available in the online journal.)

we find that the pixel-based algorithm overcorrects the CTI. This overcorrection provides evidence for the ACS CTI mitigation in the low flux regime first reported by Jee et al. (2009).

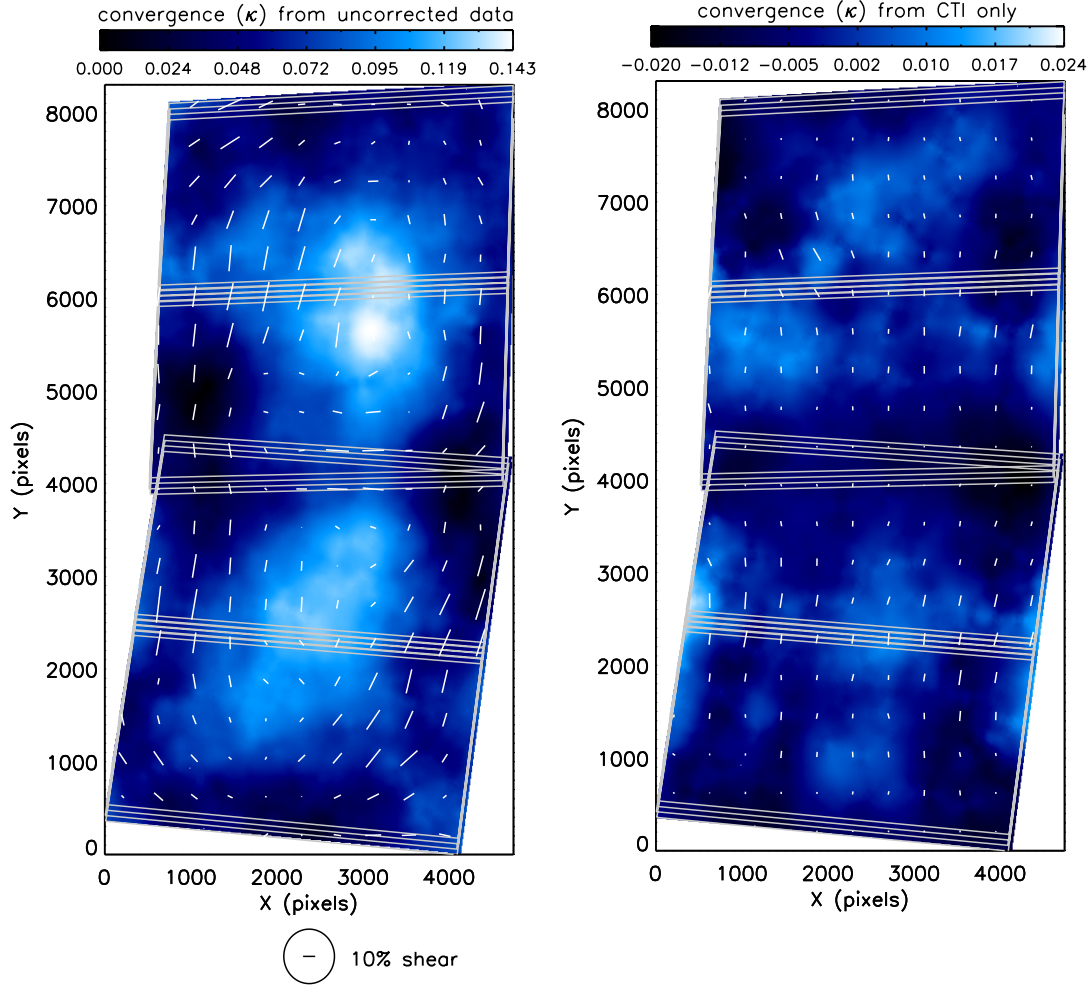### A.2. Impacts on Galaxy Shapes

Having examined the CTI using the SSFs before and after the correction, we now turn to the question: whether or not the current pixel-based correction is sufficient for our weak-lensing study of ACT-CL J0102−4915. In other words, we need to investigate if there should be additional correction to our galaxy shape measurements in order to remove the residual CTI effects shown in the right panel of Figure 18. To answer this question, we must quantify the impacts of the residual CTI effects on our source galaxy ellipticity and examine the level of the statistical noise with respect to that of the systematic noise caused by the residual CTI.

As a first step toward this goal, we perform a weak-lensing analysis of ACT-CL J0102−4915 using the CTI-uncorrected (i.e., FLT) images. The basic image reduction, PSF correction, and shape measurement methods are identical to those described in Sections 3.3 and 3.4. The left panel of Figure 19 displays this result. Despite the large CTI-induced systematic errors, it is remarkable that the bimodal distribution of the mass is clearly seen even in this weak-lensing analysis with the uncorrected data. However, direct comparison with Figure 5 (the result obtained from the FLC images) reveals that the substructures are severely smeared and distorted. In particular, the centroid of the SE cluster is no longer prominently defined in Figure 19. The difference between the two results is also obvious when we compare the whiskers computed from the smoothed ellipticity of source galaxies. In the right panel of Figure 19, we show the whiskers and resulting mass reconstruction using the differential ellipticities of the same source galaxies between the two catalogs (before and after the CTI correction). Both the direction and size

distribution of the whiskers are consistent with our expectation. That is, the orientation of the whiskers is parallel to the readout direction, and the sizes of the whiskers are largest at the center of the two ACS pointings. The difference in galaxy ellipticity provides the key information for us to relate the CTI measured with SSFs to the systematic shear in galaxies. Because galaxies are much larger than SSFs, the amount of ellipticity change in galaxies due to CTI is smaller than that in SSFs. The differential ellipticity (Figure 19) shows that a mean galaxy ellipticity change near the center of each ACS pointing is $\gamma \sim 0.08$, which is $\sim$27% of the CTI-induced ellipticity in SSFs. Without the Ubeda & Anderson (2012) pixel-based CTI correction, our shears near the center of each ACS pointing would be biased by $\gamma \sim 0.08$.
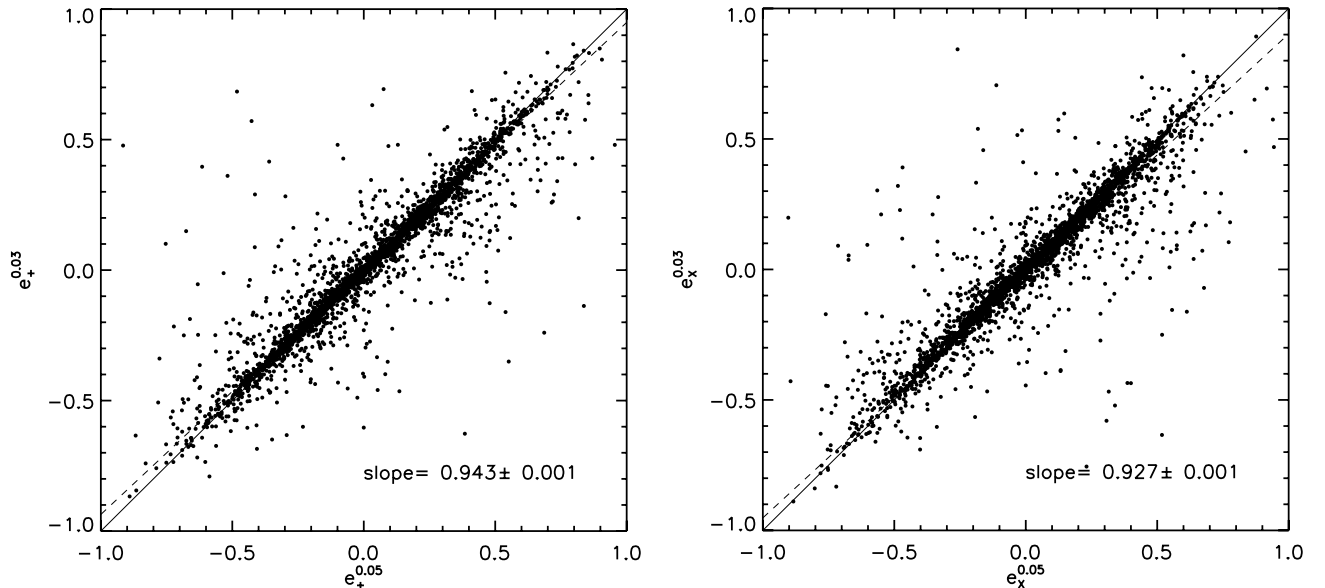
Now with this conversion factor at hand, we can estimate the residual CTI effect on galaxy shears after the pixel-based correction is carried out. For the bright SSFs ($>$300 e^{-1}), the residual is small, giving at most an ellipticity of $\sim$0.02 (Figure 18). Thus, we can neglect the impact of the residual CTI for bright galaxies. For the faint SSFs ($<$300 e^{-1}), the maximum residual ellipticity is $\sim$0.08. Applying the conversion factor of $\sim$27%, we expect that the faint galaxies will be stretched by $\delta\gamma \sim 0.02$ near the ACS pointing boundaries. If we conservatively assume that the magnitude range of the galaxies affected by this CTI overcorrection is F775W $\gtrsim$ 26.5, about $\sim$30% of our source galaxies ($\sim$800 out of 2541) are affected. Therefore, we estimate that the maximum shear systematic error induced by the residual CTI is less than $\gamma < 0.01$. One caveat is that the faint (F775W $\gtrsim$ 26.5) galaxies are smaller, and their conversion factor may become larger than our average value. However, these faint galaxies are also downweighted in our shear estimation. Our study suggests that the two effects nearly cancel each other. Because the above maximum shear systematic error $\gamma < 0.01$ is insignificant compared to the level of the statistical noise and the large cluster lensing signal, we conclude that the current pixel-based CTI correction is sufficient for our weak-lensing analysis.
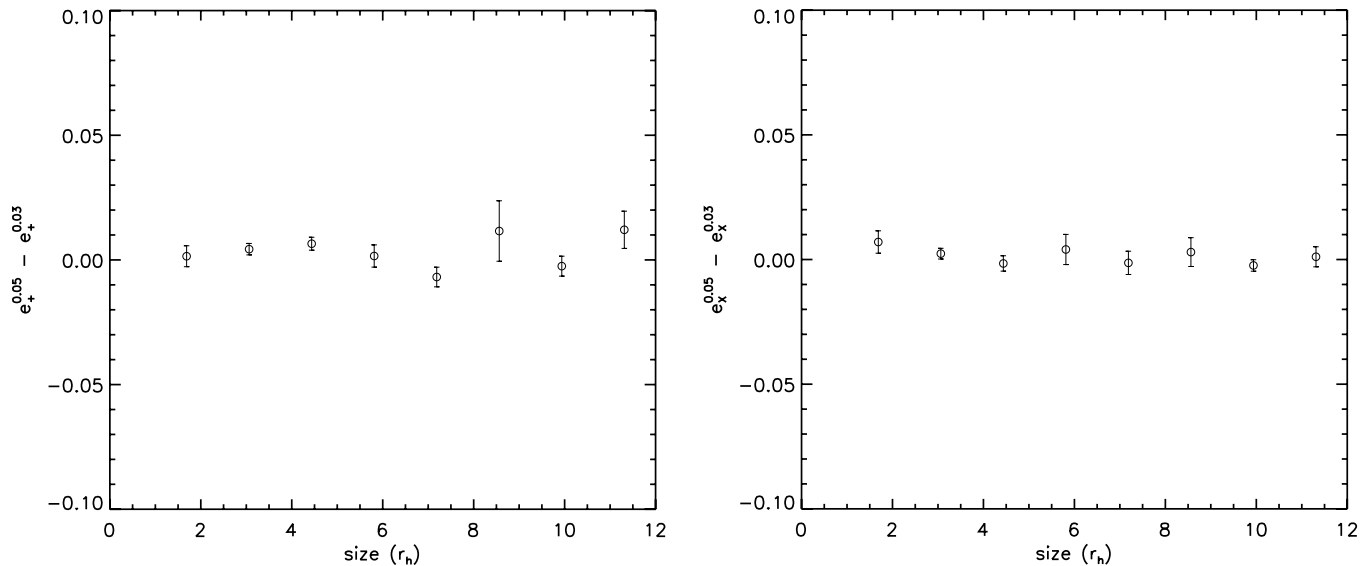
Figure 19. CTI effects on the weak-lensing analysis. The left panel shows the shears (sticks) and the corresponding mass reconstruction (blue) from the raw ACT-CL J0102−4915 images. Comparison of this result with the one shown in the left panel of Figure 5 illustrates that the global features of ACT-CL J0102−4915 is still seen in the CTI-contaminated data, although the details differ. In the right panel, we subtract the CTI-corrected ellipticities of galaxies from the uncorrected ellipticities, and smooth the results with a FWHM = 30″ Gaussian kernel (as is done in Figure 5). The spatial variation of the residual ellipticity is consistent with the theoretical expectation and also the results from the SSF test (Figure 18). The largest CTI-induced systematics ($\gamma \sim 0.1$) is seen near the boundaries of the two ACS CCDs (WFC1 and WFC2), where the distance to the readout register is longest.

(A color version of this figure is available in the online journal.)

Figure 20. Comparison of ellipticity components between the two data reductions. The superscript (0.05 or 0.03) represents the output pixel scale. The results from the two drizzling products are consistent, although there are indications that the ellipticity from the 0″03 output scale is systematically smaller (i.e., the slopes are less than unity). The solid line shows the $y = x$ equality while the dashed line is the fit to the data.

Figure 21. Ellipticity difference as a function of object size. If the impact of the drizzling output scale on the mitigation of aliasing is large, we expect to observe a trend that depends on the object size. However, we do not detect such a pattern.

APPENDIX B
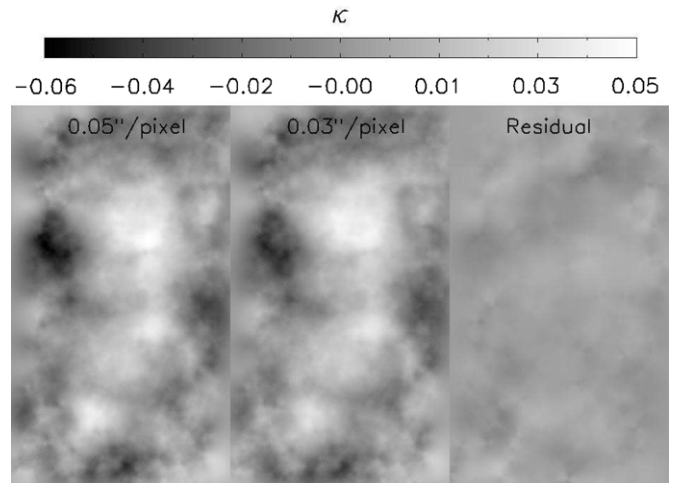
IMAGE DRIZZLING METHOD AND WEAK-LENSING PERFORMANCE

The *HST*/ACS PSFs are slightly undersampled, exhibiting some non-negligible aliasing effects. To reduce this artifact, some studies suggest drizzling WFC images with an output pixel scale smaller than the native pixel scale $0\rlap{.}''05$. We investigate the impact of the drizzling method on our weak-lensing results by performing a separate data reduction and examining the difference in the results.

We note that although the analysis presented here is performed using the PROP 12755 data set, the result holds for the entire data set (PROP 12755 and 12477). We follow the COSMOS data reduction scheme (Koekemoer et al. 2007). Namely, the output pixel scale, the pixfrac parameter, and the drizzling kernel are set to $0\rlap{.}''03$, 0.8, and Gauss.

One of the most straightforward comparisons is to crosscheck the ellipticity of the common objects as displayed in Figure 20. The results from the two versions of the ACT-CL J0102−4915 images are highly consistent. The small scatter implies that one would not reach a significantly different conclusion because of the difference in the image output scale. However, we find that the ellipticity is slightly lower in the $0\rlap{.}''03$ output scale, as indicated by the fitted slopes (dashed) being less than unity. This means that for the conversion of ellipticity to shear we need to apply a larger shear calibration factor. The exact cause for this difference in shear calibration is not clear at the moment.

Another useful diagnostic is the investigation of the ellipticity difference between the two versions of the data reduction as a function of object size. If the aliasing arising from undersampling is severe and can be relieved by the choice of the $0\rlap{.}''03$ output scheme, we expect to detect some systematic difference in ellipticity for small objects. However, as shown in Figure 21, no obvious size-dependent pattern is present.

Finally, we compare the scientific results from the two versions of the data reduction. We find that the two weak-lensing masses agree within ∼2% when we apply the corresponding shear calibration factor to each shear catalog. The 2D mass maps are compared in Figure 22. We select common source galaxies
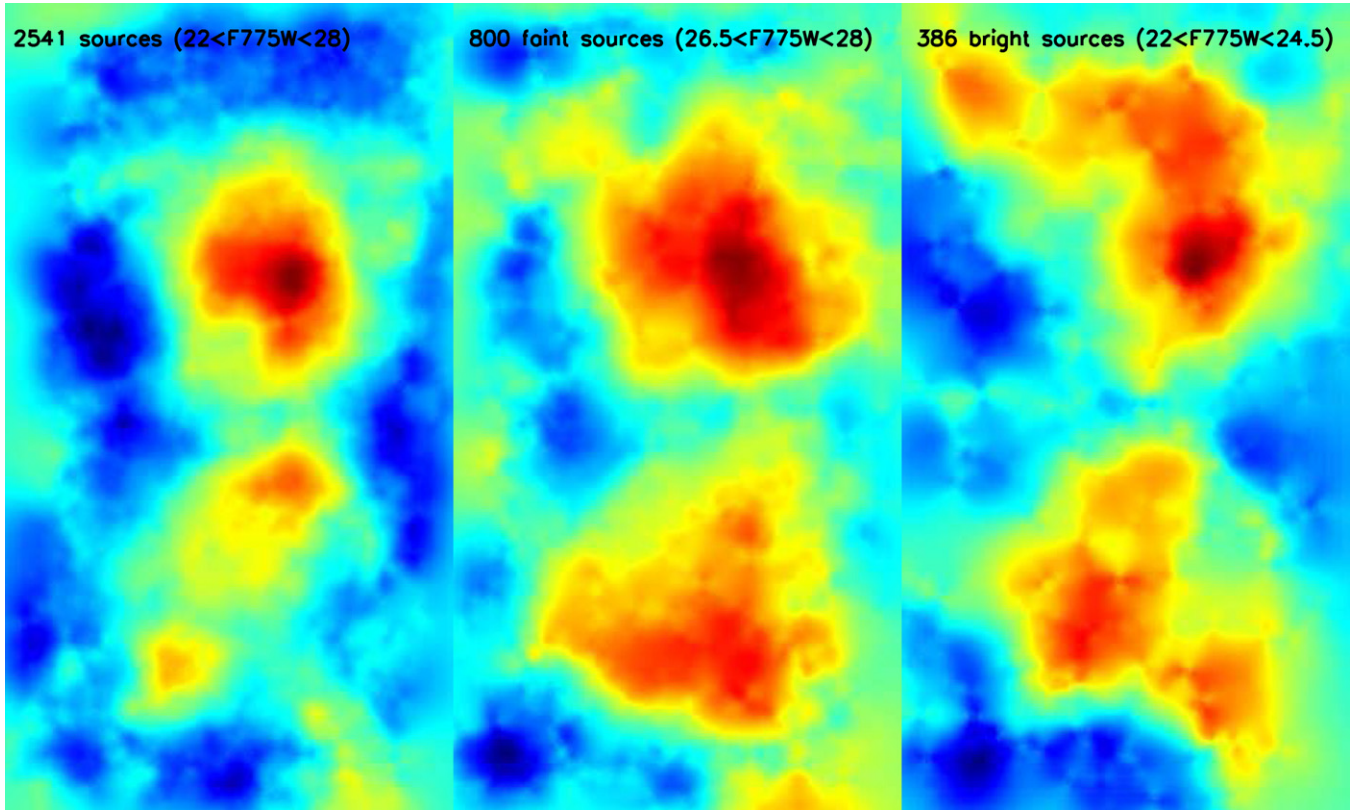

Figure 22. Comparison of two-dimensional mass reconstructions from the two data reductions. We use FIATMAP to produce the result. The common source galaxies are selected by looking for pairs within ∼$0\rlap{.}''15$ after the application of the criteria in Section 3.5. The results are in excellent agreement. Because here we do not apply the corresponding shear calibrations, the agreement can become even better when this remaining correction is applied.

by looking for pairs within ∼$0\rlap{.}''15$ after applying the criteria in Section 3.5. The results are in excellent agreement as indicated by the small residual across the field of view (right). Because here we do not apply the corresponding shear calibration to each ellipticity catalog, the agreement can be made even better by applying this remaining correction.

APPENDIX C

MAGNITUDE-DEPENDENT LENSING SIGNAL

We select source population in a broad magnitude range (e.g., 22 < F775W < 28 where F775W is available). One may question whether these lower and upper bounds are legitimate choices. In case the faint end is too faint, our source selection is severely contaminated by too noisy (thus unusable) galaxies, which dilute the cluster lensing signal. Likewise, in case the

Figure 23. Mass reconstruction with sources of different magnitudes. We define two sub-samples by applying different magnitude limits. The mass reconstruction using the entire source population is displayed in the left panel. This mass map is created with FIATMAP and is slightly different from the maximum entropy mass map presented in Section 4.1. The middle and right panels show the results from the bright and faint sources, respectively. These two mass maps are much noisier because of the considerably smaller number of sources. However, it is easy to identify the bimodal mass distribution of ACT-CL J0102−4915 in both cases.

(A color version of this figure is available in the online journal.)

bright end is too bright, the population at the bright end is mostly cluster galaxies or foreground objects containing no lensing signal. Therefore, here we demonstrate that our sources at both ends provide significant lensing signals and add to the overall S/N of our measurements.

Within the area defined by the ACS pointings of the PROP 12755, the total number of sources is 2541. The mass reconstruction using the entire source population is displayed in the left panel of Figure 23. This mass map is created with FIATMAP without implementing the non-linear relation ($g = \gamma/(1 - \kappa)$) between shear and ellipticity and is slightly different from the maximum entropy mass map presented in Section 4.1. Then, we separate faint sources by selecting objects in the $26.5 <$ F775W < 28 range. This sub-sample contains 800 galaxies, and the corresponding mass map is shown in the middle panel. In addition, we define a bright sample using the $22 <$ F775W < 24.5 magnitude range. The total number of sources in the bright sample is 386. The resulting mass map is shown in the right panel. The two mass maps created from these two sub-samples are much noisier because of the considerably smaller source densities. However, it is easy to identify the bimodal mass distribution of ACT-CL J0102−4915 in both cases. Thus, both sub-samples contain significant lensing signals, which serve as justification for our choice of the magnitude limits.

REFERENCES

Anderson, J., & Bedin, L. R. 2010, PASP, 122, 1035
Bartelmann, M. 1996, A&A, 313, 697
Becker, M. R., & Kravtsov, A. V. 2011, ApJ, 740, 25
Beckwith, S. V. W., Stiavelli, M., Koekemoer, A. M., et al. 2006, AJ, 132, 1729
Bennett, C. L., Larson, D., Weiland, J. L., et al. 2013, ApJS, 208, 20
Bernstein, G. M., & Jarvis, M. 2002, AJ, 123, 583
Bertin, E., & Arnouts, S. 1996, A&AS, 117, 393
Bridle, S. L., Hobson, M. P., Lasenby, A. N., & Saunders, R. 1998, MNRAS, 299, 895
Brodwin, M., Gonzalez, A. H., Stanford, S. A., et al. 2012, ApJ, 753, 162
Cayón, L., Gordon, C., & Silk, J. 2011, MNRAS, 415, 849
Clowe, D., Bradač, M., Gonzalez, A. H., et al. 2006, ApJL, 648, L109
Coe, D., Benítez, N., Sánchez, S. F., et al. 2006, AJ, 132, 926
Dahlen, T., Mobasher, B., Dickinson, M., et al. 2010, ApJ, 724, 425
Dawson, W. A., Wittman, D., Jee, M. J., et al. 2012, ApJL, 747, L42
Duffy, A. R., Schaye, J., Kay, S. T., & Dalla Vecchia, C. 2008, MNRAS, 390, L64
Eddington, A. S. 1913, MNRAS, 73, 359
Fahlman, G., Kaiser, N., Squires, G., & Woods, D. 1994, ApJ, 437, 56
Fischer, P., & Tyson, J. A. 1997, AJ, 114, 14
Foley, R. J., Andersson, K., Bazin, G., et al. 2011, ApJ, 731, 86
Giavalisco, M., et al. 2004, ApJL, 600, L93
Gonzalez, A. H., Stanford, S. A., Brodwin, M., et al. 2012, ApJ, 753, 163
Hao, J., Kubo, J. M., Feldmann, R., et al. 2011, ApJ, 740, 39
Harrison, I., & Coles, P. 2012, MNRAS, 421, L19
Harrison, I., & Hotchkiss, S. 2013, JCAP, 07, 022
Hasselfield, M., Hilton, M., Marriage, T. A., et al. 2013, JCAP, 7, 8
Hoekstra, H. 2007, MNRAS, 379, 317
Hotchkiss, S. 2011, JCAP, 07, 004
Hoyle, B., Jimenez, R., & Verde, L. 2011, PhRvD, 83, 103502
Jee, M. J., Blakeslee, J. P., Sirianni, M., et al. 2007a, PASP, 119, 1403
Jee, M. J., Dawson, K. S., Hoekstra, H., et al. 2011, ApJ, 737, 59
Jee, M. J., Ford, H. C., Illingworth, G. D., et al. 2007b, ApJ, 661, 728
Jee, M. J., Rosati, P., Ford, H. C., et al. 2009, ApJ, 704, 672
Jee, M. J., Tyson, J. A., Schneider, M. D., et al. 2013, ApJ, 765, 74
Jee, M. J., White, R. L., Benítez, N., et al. 2005a, ApJ, 618, 46
Jee, M. J., White, R. L., Ford, H. C., et al. 2005b, ApJ, 634, 813
Jimenez, R., & Verde, L. 2009, PhRvD, 80, 127302

Kaiser, N., & Squires, G. 1993, ApJ, 404, 441
Kaiser, N., Squires, G., & Broadhurst, T. 1995, ApJ, 449, 460
Kinney, A. L., Calzetti, D., Bohlin, R. C., et al. 1996, ApJ, 467, 38
Koekemoer, A. M., Aussel, H., Calzetti, D., et al. 2007, ApJS, 172, 196
Koekemoer, A. M., Fruchter, A. S., Hook, R. N., & Hack, W. 2002, in The 2002
    HST Calibration Workshop, ed. S. Arribas, A. Koekemoer, & B. Whitmore
    (Baltimore, MD: STScI), 337
Lindner, R. R., Baker, A. J., Hughes, J. P., et al. 2013, arXiv:1310.6786
Lombardi, M., & Bertin, G. 1999, A&A, 348, 38
Markevitch, M., Gonzalez, A. H., David, L., et al. 2002, ApJL, 567, L27
Markevitch, M., Govoni, F., Brunetti, G., & Jerius, D. 2005, ApJ, 627, 733
Marriage, T. A., Acquaviva, V., Ade, P. A. R., et al. 2011, ApJ, 737, 61
Melchior, P., & Viola, M. 2012, MNRAS, 424, 2757
Menanteau, F., Hughes, J. P., Sifón, C., et al. 2012, ApJ, 748, 7
Meneghetti, M., Fedeli, C., Zitrin, A., et al. 2011, A&A, 530, A17
Meneghetti, M., Rasia, E., Merten, J., et al. 2010, A&A, 514, A93
Merten, J., Coe, D., Dupke, R., et al. 2011, MNRAS, 417, 333
Mortonson, M. J., Hu, W., & Huterer, D. 2011, PhRvD, 83, 023015
Navarro, J. F., Frenk, C. S., & White, S. D. M. 1997, ApJ, 490, 493
Oguri, M., & Hamana, T. 2011, MNRAS, 414, 1851

Planck Collaboration, Ade, P. A. R., Aghanim, N., et al. 2013a, arXiv:1303.5089
Planck Collaboration, Ade, P. A. R., Aghanim, N., et al. 2013b, arXiv:1303.5076
Planck Collaboration, Aghanim, N., Arnaud, M., et al. 2011, A&A, 536,
    A26
Randall, S. W., Markevitch, M., Clowe, D., Gonzalez, A. H., & Bradač, M.
    2008, ApJ, 679, 1173
Refregier, A., Kacprzak, T., Amara, A., Bridle, S., & Rowe, B. 2012, MNRAS,
    425, 1951
Rocha, M., Peter, A. H. G., Bullock, J. S., et al. 2013, MNRAS, 430, 81
Schneider, M. D., Cole, S., Frenk, C. S., et al. 2013, MNRAS, 433, 2727
Seitz, C., & Schneider, P. 1997, A&A, 318, 687
Seitz, S., Schneider, P., & Bartelmann, M. 1998, A&A, 337, 325
Sifón, C., Menanteau, F., Hasselfield, M., et al. 2013, ApJ, 772, 25
Stanford, S. A., Brodwin, M., Gonzalez, A. H., et al. 2012, ApJ, 753, 164
Tinker, J., Kravtsov, A. V., Klypin, A., et al. 2008, ApJ, 688, 709
Ubeda, L., & Anderson, J. 2012, Instrument Science Report, ACS 2012-03
    (Baltimore, MD: STScI)
Waizmann, J.-C., Redlich, M., & Bartelmann, M. 2012, A&A, 547, A67
Williamson, R., Benson, B. A., High, F. W., et al. 2011, ApJ, 738, 139
Zitrin, A., Menanteau, F., Hughes, J. P., et al. 2013, ApJL, 770, L15